ORGANOMETALLICS

pubs.acs.org/Organometallics Article

Shining Light on the Solution- and Excited-State Dynamics of Chalcogenopyrylium Polymethine Dyes

Lauren E. Rosch, Matthew R. Crawley, Ryan M. O'Donnell, Thomas N. Rohrabaugh, Jr., Trenton R. Ensley, Thomas A. Sobiech, and Timothy R. Cook*

Cite This: *Organometallics* 2022, 41, 2301−2316 Read Online

ACCESS | Metrics & More | Article Recommendations | Supporting Information

ABSTRACT: Despite 40 years of interest in chalcogenopyrylium polymethine dyes, significant gaps remain in our understanding of their photophysical properties. These gaps hinder efforts to apply such dyes as photodynamic therapy and/or biomedical sensing agents where a complete understanding of their excited-state dynamics and chemistry are important. For example, despite previous reports that establish singlet oxygen yields as high as 12% for certain dyes, we observe no evidence for $^1O_2$ from direct phosphorescence measurements. We now fill in many of these gaps through steady-state and pulsed-laser kinetic experiments on a family of 14 dyes, including six novel dyes, selected to vary physical and electronic structure. These structural changes encompass the selenium and tellurium heteroatoms, phenyl, thiophene, *tert*-butyl substituents, and methine linker length. Excited-state lifetimes were obtained by femtosecond transient absorption spectroscopy. Lifetimes were all sub-300 ps, suggesting rapid relaxation out of their excited states. Notably, we observed no evidence of any triplet transient processes; phosphorescence was only observed in samples at 77 K. Variable-temperature NMR experiments implicate rotation of the pyran ring about the methine backbone as a critical determinant of the dynamics of these dyes that distinguishes their photophysics from more rigid analogues. Our work establishes that even within the same class of compounds (*e.g.*, pyrylium dyes), properties and reactivities may differ significantly yet the origins of these differences are not apparent from photophysical measurements alone. When combined with studies of structural dynamics, we have obtained a complete structure−function relationship that we can now apply to much broader classes of dyes and serves as a reliable foundation for developing the applications of such species.

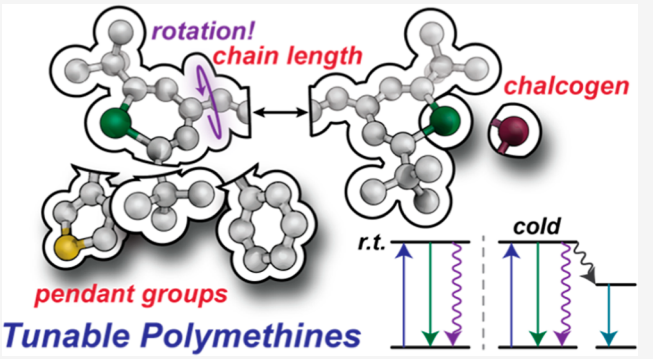

INTRODUCTION

Chalcogenopyrylium polymethine (CPP) dyes were first reported in 1988.[1] They consist of two chalcogen-containing six-membered heterocycles, traditionally named chalcogenopyrylium and chalcogenopyran cores, linked through three or more methine moieties illustrated in Figure 1. These dyes have tunable scaffolds that allow for direct structural changes that result in altered photophysics. This facile tuning makes them useful in photodynamic therapy,[2−8] solar energy conversion,[9] and biomedical imaging.[10−16] Explorations of the applications of these dyes have outpaced fundamental studies of their photophysical properties, which remain underdeveloped. Detty and co-workers have established certain aspects of the electronic structure of mono- and trimethine CPP dyes.[1,9,11,17] The same tuning that makes them attractive for applications can be used for systematic studies of photophysics. As such, these structures are amenable to the introduction of different chalcogens (E), lengthening the methine backbone, or substituting various aliphatic or aromatic functionalities to the core (R). For example, it has been established that modifying the chalcogen or methine backbone results in a 100−120 nm (~1500 cm^{-1}) shift in absorption maxima.[17,18]

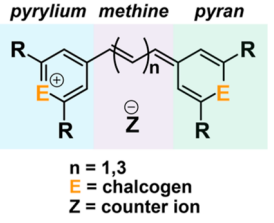

Figure 1. General structure of CPP dyes. When n = 1, trimethine; n = 3, pentamethine.

Received: June 1, 2022
Published: August 9, 2022

https://doi.org/10.1021/acs.organomet.2c00263
Organometallics 2022, 41, 2301−2316

This level of understanding is sufficient to tune absorption maxima to align with excitation wavelengths for biomedical imaging, but falls short of providing a complete understanding of the nature of the photophysics of these dyes.

In general, CPP dyes are reported to have small fluorescence quantum yields, $\Phi_{FL,}$ and singlet oxygen quantum yields, $\Phi(^1O_2)$, of 15% or less. Thus, the dominant pathway out of the excited state is non-radiative in nature though these other processes do contribute. The ramifications of molecular motion on these pathways have been explored in a small number of studies on CPPs and related dyes.[19−21]

We became particularly interested in the ability of these dyes to act as sensitizers for singlet oxygen because that property has motivated their study as photocatalysts and photodynamic therapy agents. Trimethine dyes of this type are reported to produce singlet oxygen upon irradiation in air-saturated solutions,[7,22,23] but these reports are all based on indirect methods where the evidence for $^1O_2$ could be due to other reactive oxygen species or reaction pathways. While exploring this chemistry further, we realized that although a number of CPP dyes have been reported, there has been no systematic study of their structural and excited-state dynamics.

Herein, we explore the electronic structure and excited-state dynamics of 14 dyes, including six novel dyes. Our wide design space addressed changes to the selenium and tellurium heteroatoms; the pendant *t*-butyl, phenyl, and thiophene substituents; and the length of the polymethine backbone, variations that were all confirmed *via* single crystal X-ray diffraction studies. A series of VT-NMR experiments provided a deeper understanding of the nature and kinetics of molecular motion, whereas femtosecond transient absorption (fsTA) and 77 K emission spectroscopies were used to interrogate excited-state dynamics. The results of these techniques provide a complete and consistent understanding of CPP dyes that serves as a basis for discussing pyrylium species in general.

RESULTS AND DISCUSSION

Synthesis. Polymethine chalcogenopyrylium dyes were synthesized from key dye precursor pyrylium salts. The synthesis of selenopyrylium and telluropyrylium dyes, illustrated in Scheme 1, follow modified methods reported in the literature.[1] Full synthetic details of all dye precursor molecules are outlined in the Supporting Information. Trimethine CPP dyes have three methine moieties bridging the two chalcogenopyran cores.

The condensation of 4-methylchalcogenopyrylium salts with (chalcogeno-pyranlidene)acetaldehydes bearing the same chalcogen heteroatom and desired R-groups, in 105 °C acetic anhydride for 5−30 min yielded trimethine dyes **T1-SePh**, **T2-TePh**, **T3-Se3Th**, **T4-Se2Th**, **T5-Se^{t}Bu**, and **T6-Te^{t}Bu** with yields ranging between 64 and 95%. Throughout this article, we will use the following naming convention, **XN-ER**, where **X** refers to either **T** (trimethine) or **P** (pentamethine), **N** refers to the index of the dyes (*e.g.*, 1−6), **E** refers to either **Se** or **Te**, and **R** refers to the functional groups of the pyran ring. Treating 4-methylchalcogenopyrylium salts with (chalcogeno-pyranlidene)acetaldehydes containing different chalcogen heteroatoms, produced asymmetric trimethine dyes, **T1.5-SeTePh** and **T5.5-SeTe^{t}Bu** in 90 and 64% yields, respectively. To avoid heteroatom scrambling,[24] which forms the undesired symmetric analogue, the reaction times for the asymmetric trimethine dyes were kept under 2 min. One way to lengthen the methine bridge between the two chalcogenopyran cores is to use a cyanine compound[25,26] as the extended methine source. Pentamethine chalcogenopyrylium dyes **P1-SePh**, **P2-TePh**, **P3-Se3Th**, **P4-Se2Th**, **P5-Se^{t}Bu**, and **P6-Te^{t}Bu** were prepared by condensing 4-methylchalcogenopyrylium salts, decorated with desired R-groups, with cyanine in a 1:1 mixture of acetic acid/acetic anhydride in the presence of sodium acetate as a base. Yields ranged from 14 to 79%. All dyes were recrystallized from acetonitrile or from acetonitrile/diethyl ether.

Scheme 1. General Synthesis of Chalcogenopyrylium Tri- and Pentamethine Dyes

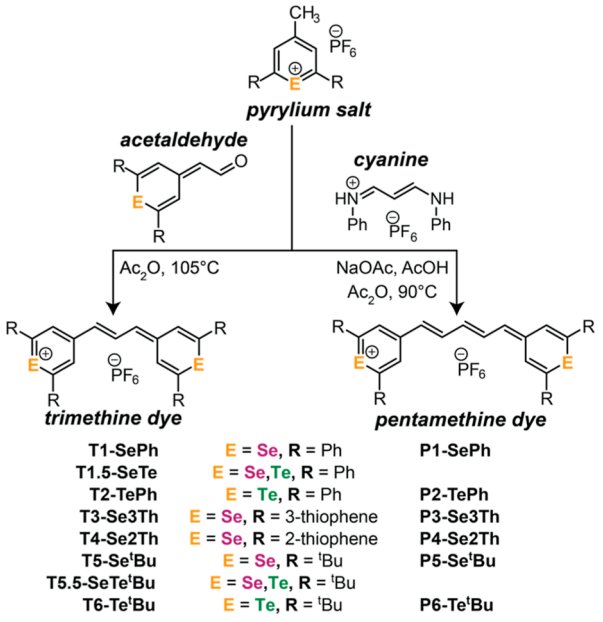

NMR Characterization. The ^{1}H NMR spectra of all trimethine dyes show a downfield triplet (∼8.50 ppm; Figure 2, red) corresponding to the central methine proton; as well as a doublet (∼7.00 ppm, Figure 2, blue) corresponding to the other methine protons, along with any aromatic or aliphatic proton resonances from the R-groups. The mixed chalcogen dyes have a doublet of doublets (∼6.80 ppm, Figure 2, blue) showing that the two methine protons closest to the chalcogenopyran cores are inequivalent. The pentamethine dyes all show a triplet (∼8.30 ppm, Figure 2, teal), a doublet of doublets (∼6.80 ppm, Figure 2, red), and a doublet (∼6.70 ppm, Figure 2, blue) corresponding to the methine protons. In both trimethine and pentamethine dyes, there are broad singlets around 7.50 ppm (Figure 2, orange) that correspond to the pyran protons. At room temperature, this resonance is broad, and in some of the dyes, particularly the pentamethine series, is indistinguishable from the baseline, a phenomenon we explain based on our VT-NMR results.

A lack of ^{13}C NMR data in prior reports on dyes of this type is an indication that standard carbon NMR conditions often yield unsatisfactory results.[27,28] Nonetheless, we were able to obtain informative data under specific conditions that will be discussed in the VT-NMR section below. Additional details of the characterizations of the dyes can be found in the Supporting Information.

Electrospray Ionisation Mass Spectrometry. Electrospray ionization Fourier transform ion cyclotron resonance mass spectrometry (ESI-FT-ICR MS) further supports the formation of all dyes. Figure 4 shows a representative example

https://doi.org/10.1021/acs.organomet.2c00263
Organometallics 2022, 41, 2301−2316

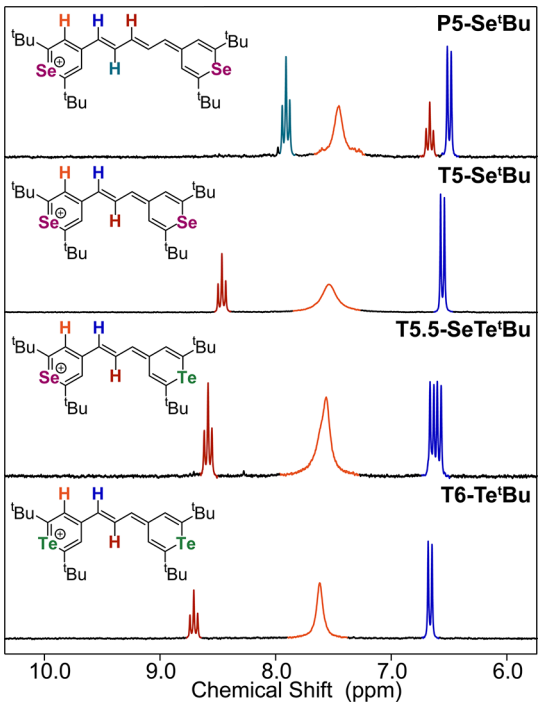

Figure 2. Aromatic region of ^{1}H NMR spectra (25 °C) of a representative sample of CPP dyes in CD_2Cl_2.

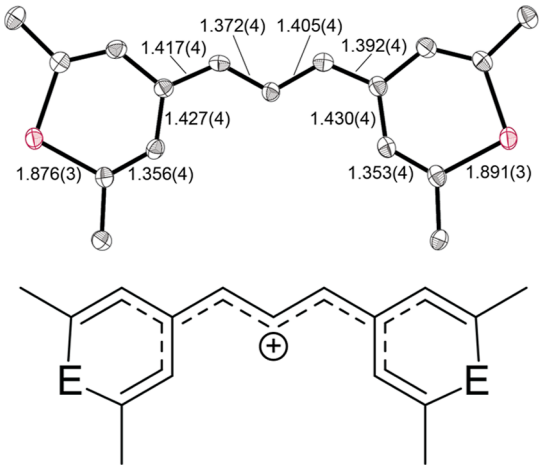

Figure 3. Crystallographically determined bond lengths of **T1-SePh** that support the resonance delocalization shown below. Hydrogen atoms, carbons of phenyl substituents, and PF_6^- counterions have been omitted for clarity.

of ESI-FT-ICR MS data obtained for these compounds. Across the entire series, the main species observed were the cationic dyes without their PF_6^- counterions, denoted $[M - PF_6^-]^+$. Interestingly, when obtaining a mass spectrum for **T6-Te^{t}Bu**, an additional tellurium-containing peak was observed (Figure S82). The second peak was consistent with a Te/O asymmetric trimethine polymethine dye, which was supported by simulation. There is literature precedent for a tellurium-oxygen exchange when a superoxide radical anion reacts with these dyes.[2] We hypothesize that superoxide may be generated during the ESI stage of the mass spectrometer, giving rise to the tellurium-oxygen species observed. There is no evidence of the scrambled Te/O asymmetric dye in the UV−vis spectrum or NMR spectrum.

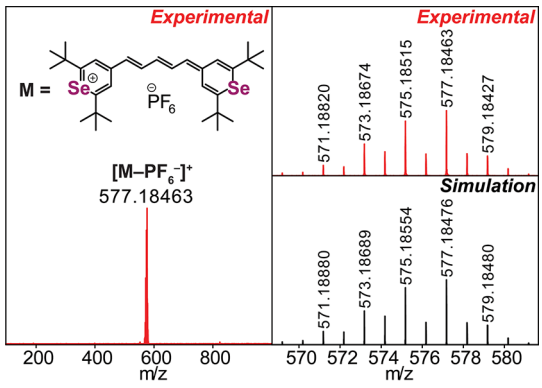

Figure 4. ESI-FT-ICR mass spectrum of **P5-Se^{t}Bu** (acetonitrile).

Crystallography. Thus far, there have been only three reported crystal structures of CPP dyes.[1,10,29] In each report, only a single structure was reported with no major comparisons made. Herein, we reported 10 new crystal structures, including the first examples of Te-containing polymethine dyes (Figure 5). In all structures, the chalcogenopyrylium rings are planar, with no major displacement of the heteroatom from the plane defined by the carbon atoms. A survey of the pyrylium/pyran rings in each of the crystal structures provides insights into the nature of bonding. The C−E bonds are slightly contracted from the expected C−E single bond lengths. The C−C bonds adjacent to C−E bonds show substantial double bond character (typical C=C of 1.34 Å).[30] The average C−C bond lengths are 1.354(7) and 1.354(8) Å when E is Se and Te, respectively. Finally, the C−C bonds which lead into the methine backbone are both 1.43(1) Å on average (for both Se- and Te-dyes), almost exactly halfway between a typical C−C and C=C bond. Both chalcogenopyrylium rings within a single dye are symmetric, that is, there is no major difference in bond lengths between rings. This brings into question the resonance structures for this class of dye. Typically, the dye is drawn with a formal positive charge on the chalcogen atom forming a pyrylium ring. The other is drawn as a neutral pyran ring. There of course exists a second resonance structure where the pyrylium and pyran rings are flipped; however, if these were the only two "resonance contributors," we would expect to find more uniform C−C bond lengths within the rings, rather than the observed formal double bonds. There is no doubt that the positive charge is delocalized through the π-system; however, it seems that the true nature of the bonding cannot be described with a simple two Lewis structure resonance pair as is often portrayed.[17,18] Moving to the methine backbone, in the case of the trimethine series, a notable alternating long-short pattern was observed in C−C bond lengths. This trend does not translate to the pentamethine series, which seem to have far more uniform C−C bond lengths. On average, methine bond lengths were approximately 1.39 Å for both tri- and pentamethine dyes; however, the standard deviation on bond lengths for the trimethine series was roughly twice that of the pentamethines. This suggests a greater degree of delocalization in the pentamethines, whereas the trimethines exhibit more "butadiene"-like bonding (see Figure 3).

Structurally, the main difference between Se- and Te-containing dyes is the C−E−C bond angle. Te-containing dyes possess a more acute bond angle, consistent with the larger ionic radius of Te compared to Se. Curiously, there is a notable

https://doi.org/10.1021/acs.organomet.2c00263
Organometallics 2022, 41, 2301−2316

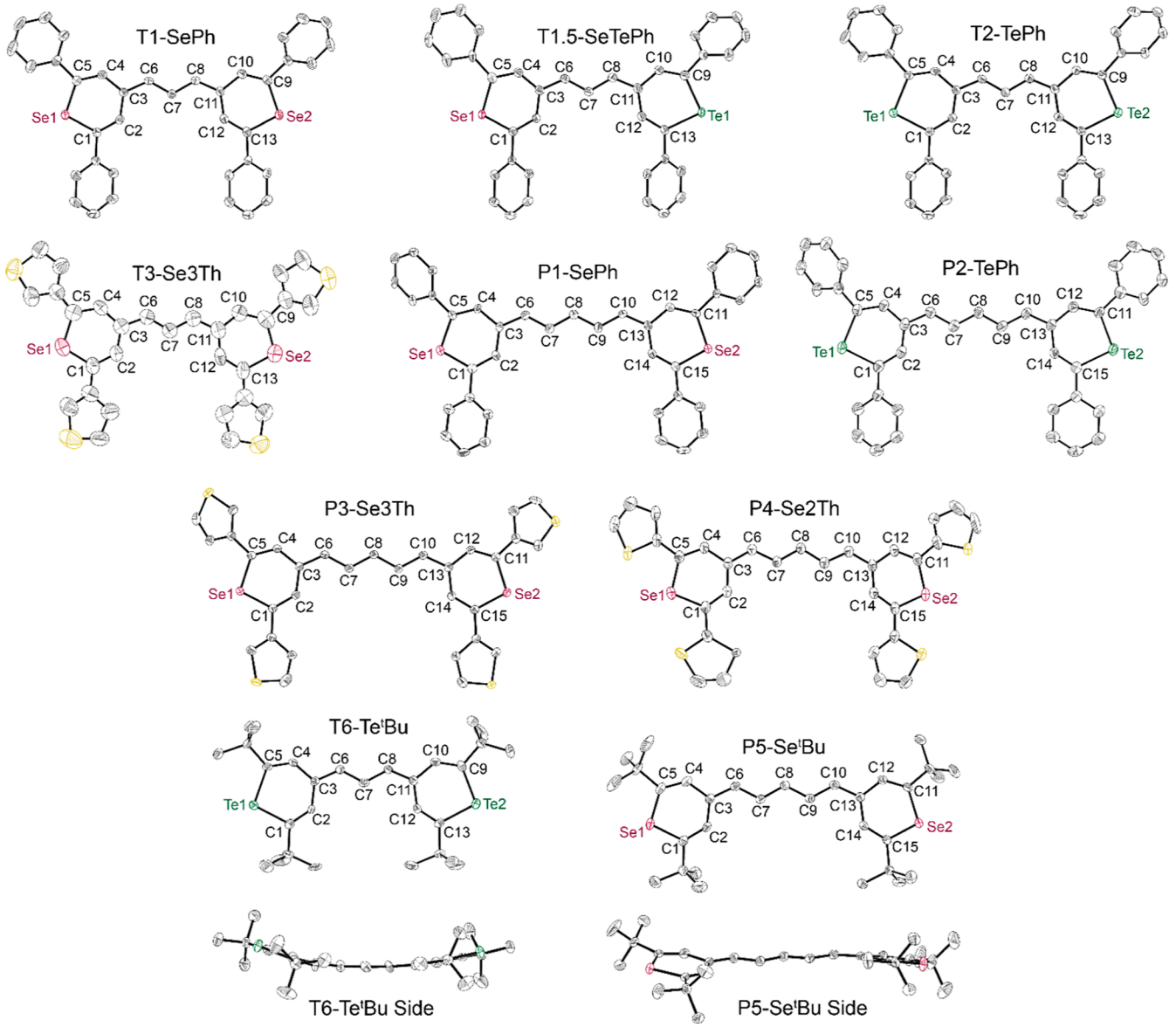

Figure 5. Thermal ellipsoid plot of tri- and pentamethine chalcogenopyrylium dyes. Probability level set at 50%. Outer sphere counterions and solvents of crystallization have been omitted for clarity.

deviation from full-molecule planarity observed in the structures of the two crystallized ^{t}butyl dyes, **T6-Te^{t}Bu** and **P5-Se^{t}Bu**. Angles of 28.9° and 19.2° were found between vectors normal to the telluropyrylium and selenopyrylium rings, respectively; an unexpected discovery in what is anticipated to be delocalized conjugated π-systems. When compared to dyes featuring aromatic cyclic R-groups, very low plane-normal to plane-normal angles were found, averaging 3.4°. Furthermore, the molecular distortions that give rise to the deviation from coplanarity are different from the tellurium trimethine to the selenium pentamethine. The rotation of the selenopyrylium ring may help mitigate 1,3-strain between the pyrylium ring protons and the methine backbone protons. With this in mind, it is also possible that the observed conformational deviations are due to crystal packing effects due to the bulky ^{t}butyl groups. Support to this hypothesis comes from density functional theory (DFT) geometry optimizations of the two dyes. Both computed structures at nearly perfectly planar (plane-normal to plane-normal angle of ~1°), suggesting that intermolecular packing effects are the impetus for the observed geometric deviations.

Electronic Absorption and Emission Spectroscopy. The UV−vis absorption and fluorescence spectra of the chalcogenopyrylium dyes were measured in aerated acetonitrile, and the resulting parameters are summarized in Table 1. The absorption spectra of each dye showed similar bands, with ground-state absorption (GSA) lambda max (λ_{GSA}) ranging from the visible into the near-IR regime (734−985 nm). This λ_{GSA} feature corresponds to the $\pi-\pi^*$ transition and has extinction coefficients ranging 0.59−2.12 × 10^5. Each dye featured a higher energy absorption band *ca.* 400 nm. This band was broad and lower molar absorptivity.

In all dyes, a shoulder was observed at higher energies to the lambda max. We have attributed this shoulder to vibronic coupling, similar to that observed in BODIPY dyes.[31] We should note that we do not observe this transition in time-dependent DFT (TD-DFT), further supporting the vibronic coupling argument as TD-DFT will not predict vibrationally

https://doi.org/10.1021/acs.organomet.2c00263
Organometallics 2022, 41, 2301−2316

Table 1. Absorption and Emission Parameters of CPP Dyes in Acetonitrile

dye	ε ($\times 10^5$, M^{-1} cm^{-1})	λ_{GSA} (nm)	λ_{EM} (nm)
T1-SePh	1.97(3)	793	819
T1.5-SeTePh	1.78(3)	830	857
T2-TePh	1.78(2)	868	896
T3-Se3Th	2.03(7)	808	829
T4-Se2Th	1.56(5)	840	863
T5-Se^{t}Bu	2.074(9)	734	747
T5.5-SeTe^{t}Bu	2.12(2)	774	789
T6-Te^{t}Bu	2.08(2)	813	828
P1-SePh	1.748(8)	911	942
P2-TePh	0.933(4)	985	1017
P3-Se3Th	1.16(1)	927	952
P4-Se2Th	1.17(2)	963	981
P5-Se^{t}Bu	1.451(8)	847	864
P6-Te^{t}Bu	0.585(8)	926	942

coupled transitions. The emission spectra of each dye showed similar bands, with lambda max (λ_{EM}) ranging from 747 to 1017 nm. These dyes show small Stokes shifts (an example is illustrated in Figure 6) for **T1-SePh**. A few general trends were

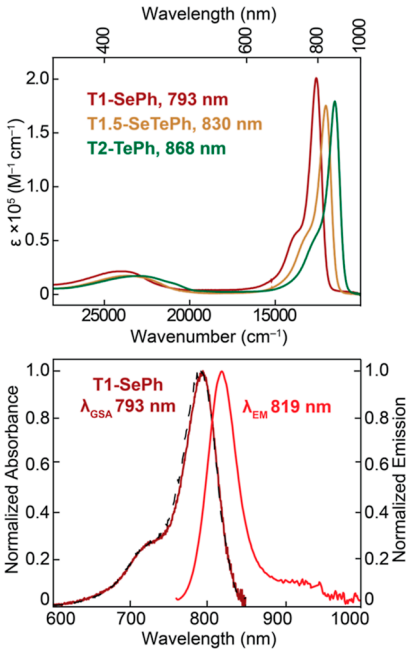

Figure 6. Top: GSA spectra of **T1-SePh**, **T1.5-SeTePh**, and **T2-TePh** in aerated acetonitrile. Bottom: room temperature emission spectrum of **T1-SePh** in aerated acetonitrile. Absorption (burgundy), emission (red, λ_{ex} = 750 nm), excitation (black dashed, λ_{em} = 860 nm).

observed. Tellurium dyes had more red-shifted absorption maxima than their selenium analogues. This trend can be explained when considering the orbital contributions to the highest occupied molecular orbital (HOMO) and lowest unoccupied molecular orbital (LUMO) from computations, as discussed below. The asymmetric dyes, **T1.5-SeTePh** and **T5.5-SeTe^{t}Bu**, had λ_{GSA} and λ_{EM} at the average of their parent symmetric dyes, shown in Figure 6. This supports frontier orbitals that have symmetric contributions across the entire molecules. If the HOMO−LUMO were more localized on a single chalcogen in one of the pyran rings, the asymmetric dyes would not fall right between the two lambda max values so precisely. There was a 1370−1820 cm^{-1} shift (113−118 nm) in λ_{GSA} and λ_{EM} when the methine backbone length was increased from a trimethine to a pentamethine. These trends are consistent with those reported in similar dye classes.[2,32] When comparing R-groups, the dyes with *t*-butyl substituents have higher energy λ_{GSA} and λ_{EM} compared to the equivalent dyes with aromatic substituents. Aromatic substituents extend conjugation, leading to the observed red-shift. For example, **T6-TetBu** with a λ_{GSA} of 813 nm compared to **T2-TePh** with a λ_{GSA} of 868 nm. Comparing the dyes with aromatic substituents, the thiophene-containing dyes have longer wavelength λ_{GSA} and λ_{EM} compared to the phenyl-substituted dyes (*e.g.*, **P3-Se3Th** *vs* **P1-SePh**). The ability of these R-groups to sit co-planar with the core and backbone determine the extent that they contribute to the HOMO and LUMO. Thus, the smaller thiophene substituents can better align, whereas the phenyl substituents are larger and rotate out of the plane of the dye. This can be seen in the crystal structures of dyes containing thiophene and phenyl substituents (see Figure 5).

77 K emission measurements were performed on aerated and freeze−pump−thaw-degassed samples of **T2-TePh** in a 50% MeOH in CH_2Cl_2 glass. A weak but measurable phosphorescence signal was observed. The lifetime of phosphorescence was measured to be less than 1 ns by time-correlated single photon counting (see the Supporting Information). Figure S103 shows the near-infrared (NIR) emission spectrum at 77 K of **T2-TePh**.

Electrochemistry. The electrochemical properties were examined by cyclic voltammetry (CV). The data are summarized in Table 2. At open circuit potential, the dyes

Table 2. Summary of Reduction Potentials of CPP Dyes

dye	$E_{3+/+}$ [a]	$E_{+/0}$ [a]	$E_{0/-}$ [a]
T1-SePh	0.443	−0.592	−1.477
T1.5-SeTePh	0.407	−0.558	−1.426
T2-TePh	0.362	−0.522	−1.375
T3-Se3Th	0.338	−0.592	−1.483
T4-Se2Th	0.397	−0.510	−1.377
T5-Se^{t}Bu	0.431	−0.810	−1.819
T5.5-SeTe^{t}Bu	0.411	−0.765	−1.759
T6-Te^{t}Bu	0.340	−0.729	−1.670
P1-SePh	0.251	−0.548	−1.477
P3-Se3Th	0.209	−0.591	−1.487
P4-Se2Th	0.259	−0.487	−1.380
P5-Se^{t}Bu	0.221	−0.751	−1.746
P6-Te^{t}Bu	0.176	−0.679	−1.643

[a] V *vs* Fc^+/Fc^0.

exist as monocations. Three primary redox events are observed. Relative to the monocation, there is a single two-electron oxidation and two one-electron reductions. $E_{3+/+}$ refers to the oxidation event. $E_{+/0}$ refers to the first reduction, and $E_{0/-}$ refers to the second (Figure 7). Tetrabutylammonium hexafluorophosphate ($TBAPF_6$) was used as the supporting electrolyte for the trimethine dyes, and tetrabutylammonium tetrafluoroborate ($TBABF_4$) for the pentamethine dyes since the pentamethine series were poorly soluble in $TBAPF_6$ solutions.

Both trimethine and pentamethine series have two reductions with peak-to-peak separations all above 59 mV

https://doi.org/10.1021/acs.organomet.2c00263
Organometallics 2022, 41, 2301−2316

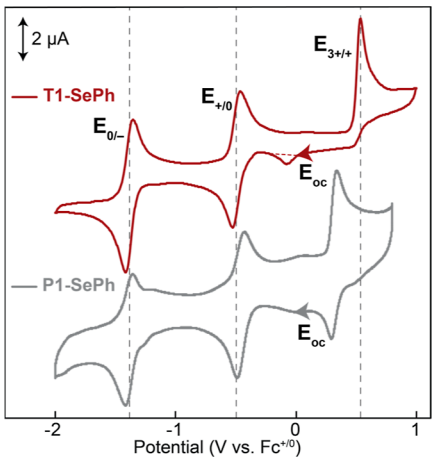

Figure 7. Cyclic voltammograms of **T1-SePh** and **P1-SePh**. All CVs were performed in acetonitrile at 0.22−0.30 mM of dye and 100 mM $TBAPF_6$ and $TBABF_4$, respectively, at a scan rate of 100 mV/s at room temperature with a glassy carbon working electrode, a 10 mM $AgNO_3$ reference electrode, and a platinum counter electrode.

that we ascribe to single-electron reductions. The peak-to-peak separations are tabulated in the Supporting Information. The $E_{1;2}$ values are shown in Table 2. The trimethine series feature irreversible oxidations between 0.20 and 0.40 V. This will be discussed in greater detail in the UV−vis spectroelectrochemistry discussion found below. In P1 through P4 pentamethine dyes, the oxidations have return waves between 0.20 and 0.25 V. The peak-to-peak separations for these events range from 28.5 to 43.7 mV suggesting two-electron processes. The trimethine series along with **P5-Se^{t}Bu** and **P6-Te^{t}Bu** have oxidation events that appear to have two return reductions.

There are some trends among the dye series. Tellurium dyes are generally easier to oxidize and reduce, which is consistent with their smaller HOMO−LUMO gaps. Lengthening the methine backbone did not significantly influence the potential of the two reductions; however, pentamethine dyes are easier to oxidize than their corresponding trimethine dyes. The mixed chalcogen dyes have oxidation and reduction events at the average of their parent symmetric analogues. These results are supported by DFT calculations vide infra and shows that the HOMO energy is dominated by methine backbone length and chalcogen identity, whereas the LUMO energy is primarily a function of R-group and chalcogen identity. These results are consistent with the red-shift in lambda max in the electronic absorption spectra observed with increasing chalcogen size and lengthening methine backbone.

UV−Vis Spectroelectrochemistry. To investigate the oxidized and reduced species of the dyes, UV−vis spectroelectrochemical experiments were performed. Figure 8 shows data for **T2-TePh** as a representative example. For all dyes, the first reduction resulted in the disappearance of the main absorption band, with simultaneous growth of a new species appearing between 468 and 575 nm. Oxidation resulted in a similar behavior, with disappearance of the lambda max band, and appearance of broad peaks between 274 and 560 nm. For trimethine dyes, the UV−vis became featureless in the spectral window after the second reduction. For pentamethine dyes, after the second reduction, a new species between 670 and 845 nm appeared. For all dyes, after cycling back to open circuit potential, the main absorption band reappeared and any new

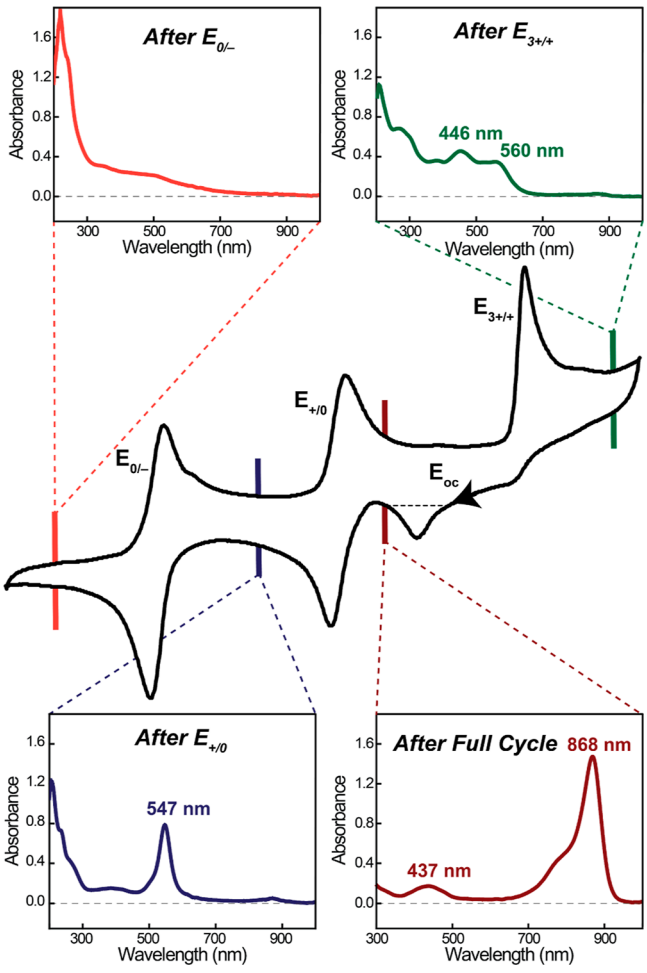

Figure 8. UV−vis spectroelectrochemistry data for **T2-TePh**. All CVs were performed in acetonitrile at 0.06 mM of dye and 100 mM $TBAPF_6$ and $TBABF_4$, respectively, at a scan rate of 100 mV/s at room temperature with a platinum working electrode, a 10 mM $AgNO_3$ reference electrode, and a platinum counter electrode.

species disappeared. See the Supporting Information for full UV−vis spectroelectrochemical data.

Computations. DFT calculations were performed to provide deeper insight into the spectroscopic and electrochemical properties of the reported chalcogenopyrylium dyes. For a complete discussion of computational details, see the Supporting Information. Geometry optimization convergence was supported by the lack of imaginary frequencies. All calculations were performed at the B3LYP level of theory using the 6-311G** and def2-SVP basis sets for Se- and Te-dyes, respectively. The optimized geometries agreed with the empirical crystal structures, in most cases with two exceptions discussed above. This supports the use of the selected functional and basis sets.

The HOMO of all dyes was a π-type orbital, while the LUMO was π^* in character. Figure 9 illustrates the frontier Mos of two representative dyes. Examining orbital parentage, the HOMO and LUMO were both dominated by the pyran ring, methine linker, and chalcogen (Figure 10). Compared to the HOMO, the LUMO showed slightly greater R-group contribution and increased contribution from the pyran ring carbon atoms at the expense of both the chalcogen and methine linker. For mixed chalcogen dyes (**T1.5-SeTePh** and **T5.5-SeTe^{t}Bu**), greater Te atomic orbital contribution was

https://doi.org/10.1021/acs.organomet.2c00263
Organometallics 2022, 41, 2301−2316

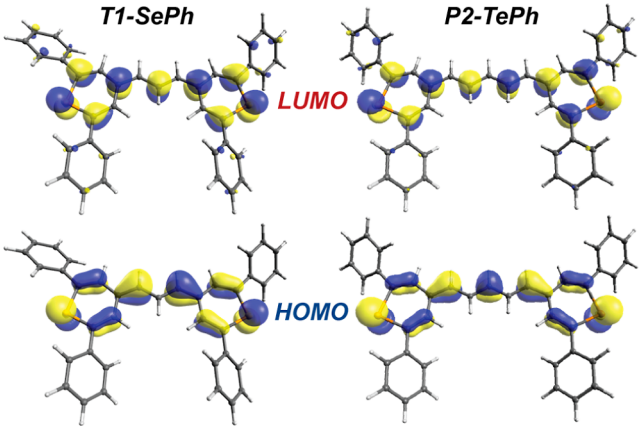

Figure 9. Frontier molecular orbitals of representative dyes.

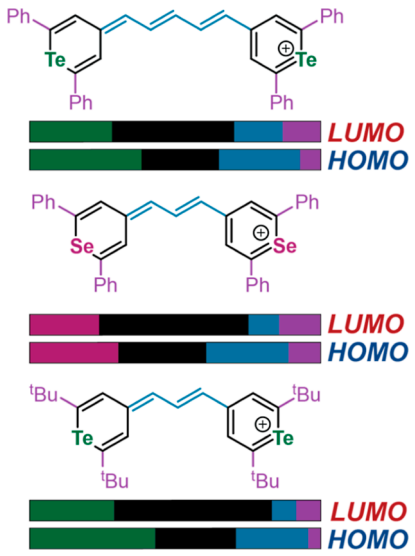

Figure 10. Frontier orbital parentage determined by DFT using the B3LYP functional with 6-311G** and def2-SVP basis sets for Se and Te, respectively.

found in the HOMO, while greater Se atomic orbital contribution was found in the LUMO. For complete orbital parentage tabulation, see Table S1.

Examining the frontier orbital energies, several trends are observed (Figure 11). Changing the chalcogen from Se to Te leads to a diminished HOMO−LUMO gap, which results from a concomitant destabilization of the HOMO and stabilization of the LUMO. Mixed chalcogen dyes were found to have orbital energies which were almost exactly the average of their parent homochalcogen dyes. Moving from an aromatic to aliphatic R-group leads to destabilization of the HOMO and LUMO; however, this effect was more pronounced with respect to the LUMO. Methine length had little effect on the LUMO energy, but lead to significant destabilization of the HOMO energy, resulting in an attenuation of the HOMO−LUMO gap by ∼0.2 eV. Notably, the calculated orbital energies support the trends predicted from electrochemical and UV−vis measurements. Indeed, oxidation events are dominated by the methine backbone length, resulting from the destabilization of the HOMO as the length increases. The greater contribution of R-groups to the LUMO is also

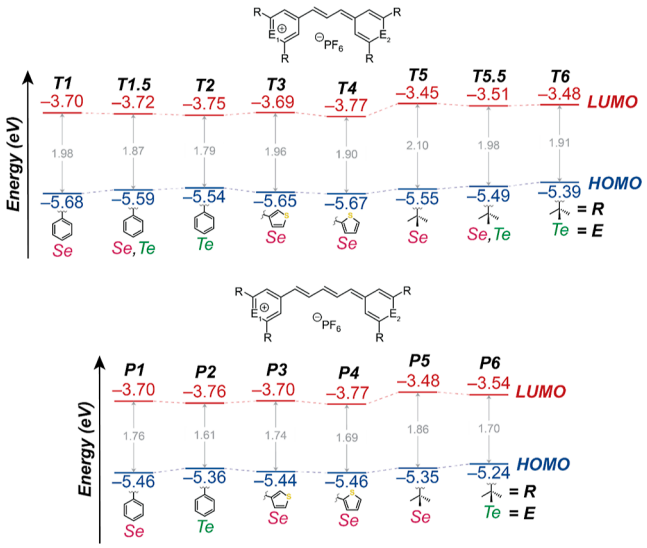

Figure 11. Tabulated HOMO−LUMO gap energies for all dye molecules. All energies are reported in eV.

supported in the electrochemical results, where reduction potentials are dominated by R-group and chalcogen identity.

TD-DFT was used to predict vertical excitation energies to simulate the electronic absorption spectra. TD-DFT calculations were also performed using the B3LYP exchange−correlation functional with the 6-311G** and def2-TZVP basis sets for Se- and Te-dyes, respectively. The results of the TD-DFT calculations suggest that the absorption maxima band for all the dyes corresponds to the $\pi-\pi^*$ transition (*i.e.* HOMO−LUMO transition). In general, TD-DFT overestimated the vertical excitation energy by ∼160 nm for trimethine and ∼210 nm for pentamethine. This is not unexpected given that TD-DFT is known to struggle with accurately estimating energies in polymethine systems.[33] Nevertheless, the relative trends' experimental absorption maxima were supported by theoretical results (Table S2). The ground-state HOMO−LUMO energy gaps also matched TD-DFT vertical excitation energy trends.

Variable-Temperature NMR. Although NMR has often been used to characterize CPP dyes, many share a spectral feature that has never been adequately explained. Specifically, the protons of the chalcogenopyran rings were found to be substantially broader than those of the other resonances associated with the dye. These broadening effects were found to be dye-dependent, as well as solvent-dependent. In some cases, the broadness resulted in the peak being nearly indistinguishable from the baseline (see the Supporting Information). Given that the broadened peaks correspond to C−H bonded protons and there is no global broadening in the spectrum, we can rule out chemical exchange and reduced molecular tumbling rates. As such, we hypothesized that solution-state dynamics could be the cause, namely, rotation of the pyran ring about the C3−C6 bond to the methine bridge (Figure 12).

To test this hypothesis, variable-temperature NMR (VT-NMR) studies were performed. Upon cooling to −70 °C, the broad pyran resonance was found to de-coalesce into two sharp resonances. This finding supports the hypothesis of rotation about the pyran-methine C3−C6 bond. At room temperature, the exchange of the two pyran protons for the reported dyes was only just beyond coalescence, in the near fast exchange regime, leading to the observed broadening.[34]

https://doi.org/10.1021/acs.organomet.2c00263
Organometallics 2022, 41, 2301−2316

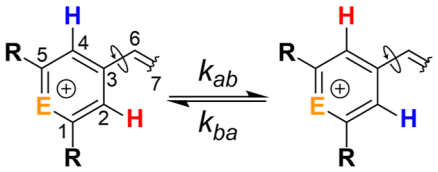

Figure 12. Rotation of the pyran ring about the methine backbone.

Upon cooling, the rate of rotation was decreased, such that the two positions with different chemical environments were observable on the NMR time scale, resulting in the two distinct peaks. If instead the NMR sample was warmed, a sharpening of the broad resonance was observed as molecular motion entered the near fast exchange regime. VT-NMR experiments were conducted in CD_2Cl_2, which allowed for low temperatures measurements; however, it precluded high temperature measurements to "fast exchange". To address this while also minimizing solvent effects from a different solvent, 1,1,2,2-tetrachloroethane was used for **P1-SePh,** which permitted substantially higher sample temperatures. This was particularly important for **P1-SePh,** given that coalescence was at room temperature, and the pyran protons were virtually indistinguishable from the baseline. For selected penta- and trimethine dyes, NMR spectra were acquired at a series of temperatures ranging from −70 to 30 °C (see the Supporting Information). Examining VT-NMR traces, several qualitative conclusions can be drawn. In general, the coalescence temperature for the phenyl- and ^{t}butyl-substituted dyes follows: Se > mixed chalcogen > Te. Furthermore, the coalescence temperature for the phenyl-containing dyes were ∼5 °C greater than the ^{t}butyl analogue. These observations suggest that changing the substituent from ^{t}butyl to phenyl, and increasing the size of the chalcogen both result in reducing the barrier toward rotation. To develop a more complete and quantitative description, NMR line shape fitting was performed.

Line shape fitting of the experiment data was performed to obtain the relevant activation parameters for the observed molecular motion (Figure 13). Figure 12 illustrates the model that was used to describe the observed line shape which can be described as a simple first-order process with equal populations. The values k_{ab} and k_{ba} represent the forward and reverse first-order rate constants. Fitting was performed in the WinDNMR software package.[35] Using the extracted first-order rate constants, activation parameters were determined using Eyring analysis. See the Supporting Information for a complete discussion of the mathematic background. The activation parameters: $\Delta H^{\ddagger}$ and $\Delta S^{\ddagger}$ were determined (see Table 3). As expected for bond rotations, the enthalpies of activation were positive; however, the entropies of activation were small and negative. This suggests that at the transition state of the rotation, energy is redistributed over a smaller number of states (*i.e.,* loss of translational, rotational, or vibrational degrees of freedom) or requires a larger solvation sphere. Selenium-containing dyes showed a greater barrier toward rotation when compared with the tellurium analogue. This is consistent with the Se-containing dyes having a higher degree of conjugation with the π-system compared to the Te-containing dyes, a ramification of the greater energetic mismatch between Te atomic orbitals and the carbon 2p orbitals. When the asymmetric mixed chalcogen dye **T5.5-SeTe^{t}Bu** was examined, the activation parameters for the Se- and Te-containing rings were fit individually. The greater error

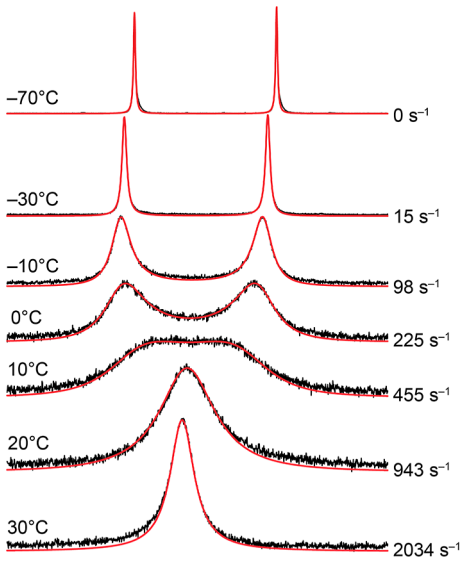

Figure 13. Experimental (black) and modeled (red) NMR peaks of the pyran protons of **T5-Se^{t}Bu**. Values on the right represent the fitted first-order rate constants for the exchange of the two pyran protons.

Table 3. Activation Parameters Determined by VT-NMR Line Shape Fitting

dye	$\Delta H^{\ddagger}$ (kcal/mol)	$\Delta S^{\ddagger}$ (cal/K·mol)
T2-TePh	11.4 ± 0.3	−5 ± 1
T5-Se^{t}Bu	11.4 ± 0.1	−6.0 ± 0.3
T5.5-SeTe^{t}Bu (Se-ring)	11.7 ± 0.5	−4 ± 2
T5.5-SeTe^{t}Bu (Te-ring)	11.2 ± 0.6	−6 ± 2
T6-Te^{t}Bu	10.6 ± 0.2	−6.7 ± 0.6
P5-Se^{t}Bu	10.3 ± 0.1	−8.9 ± 0.4

in the asymmetric dye parameters can be attributed to the greater difficulty associated with the line shape fitting because of overlapping resonances (see the Supporting Information). The obtained activation parameters followed the same trends as the symmetric dyes (*i.e.,* the Se-ring showed a greater $\Delta H^{\ddagger}$ compared to the Te-ring). When fitting **T2-TePh,** a larger activation barrier was found, which can be attributed to the larger phenyl substituents hindering rotation. VT-NMR experiments were conducted on the Se-containing phenyl-substituted dye; however, line shape analysis was hampered by overlap with the phenyl resonances. It should be noted that the similar coalescence behavior was observed (see the Supporting Information). The activation parameters of the pentamethine dye (**P5-Se^{t}Bu**) compared to the trimethine analogue showed a slightly lower enthalpy (10.3 *vs* 11.4 kcal/mol), as well as a more negative entropy (−8.9 *vs* −6.0 cal/mol·K) of activation. The substantially more negative entropy of activation suggests that solvent rearrangement is the dominating factor (*i.e.,* the larger pentamethine requires a larger solvent rearrangement to accommodate the transition state).

A dihedral scan was performed using Gaussian 09 on **T5-Se^{t}Bu,** which allowed for an approximation at the transition state geometry. The B3LYP functional and 6-311G** basis sets were used, and the highest energy geometry of the rotation process featured an approximate 90° dihedral angle between the methine and pyran ring. The starting and transition-state geometries were then optimized using ORCA 5.0.3,[36] and the Gibbs free energies of the starting and transition-state

https://doi.org/10.1021/acs.organomet.2c00263
Organometallics 2022, 41, 2301−2316

geometries were compared. The barrier to rotation was computed to be 16.2 kcal/mol. This is in good agreement with the experimental $\Delta G^{\ddagger}$ of 13.2 kcal/mol (at 298 K).

The reported Gibbs free energy of activation is also in good agreement with a previous report by Detty and Luss on variable-temperature NMR experiments of a chalcogenopyrylium trimethine dye which had been treated with bromine.[37] In their report, they suggested that the observed broadening of pyran peaks was due to the halogen ligand exchange at the Te-center; however, we propose an alternate explanation: simple rotation. They report a $\Delta G^{\ddagger}$ of 12.8 kcal/mol; however, there was a greater disparity in terms of $\Delta H^{\ddagger}$ and $\Delta S^{\ddagger}$ reported (5 kcal/mol and −26 cal/K·mol).

To aid in the total assignment of the proton NMR, low temperature 1D ROESY NMR experiments were performed (see Figure 14). Selective excitation of the first and second

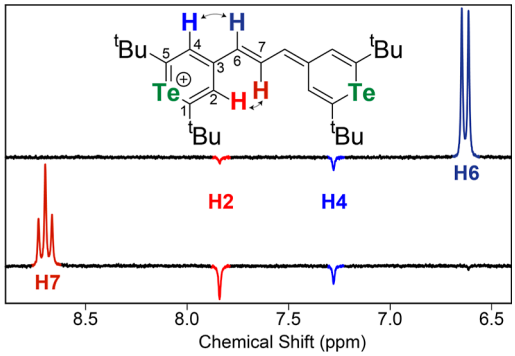

Figure 14. Selective excitation ROESY NMR spectra acquired at −60 °C in CD_2Cl_2 at 400 MHz. Upper spectrum excited at a doublet at 6.62 ppm, lower spectrum excited at a triplet at 8.69 ppm.

methine protons allowed for unambiguous assignment of the two pyran resonances observed at low temperature. Excitation of the H6 methine proton results in a NOE with H4 pyran, while excitation of the H7 methine proton shows a similar NOE with the H2 pyran proton. Interestingly, even at −70 °C, evidence of exchange was found in the ROESY spectrum. As a result, the calculated activation barrier is an upper bound, and the true activation barrier may be lower than reported. Due to increasing solvent viscosity effects at temperatures lower than −70 °C, spectra at temperatures lower were not acquired.

The dynamic behavior in solution further explains the previously reported difficulties acquiring ^{13}C NMR spectra of these dyes. The rotation leads to broadening of the resonances of carbons C1 and C5 and C2 and C4 (see Figure 12). A low temperature ^{13}C NMR spectrum was acquired at −14 °C and compared with the room temperature spectrum. A broad feature (128.49 ppm) was found to split into two sharper resonances at 131.85 and 123.89 ppm, and these resonances are due to C2 and C4. Additionally, a sharp resonance at 175.46 ppm broadened into two distinct resonances at 175.75 and 174.48 ppm, consistent with the carbons next to the Te-atom (C1 and C5). At low temperature, all carbon atoms were observable, whereas at room temperature, exchange broadening effects masked pyran (C2 and C4) ^{13}C resonances. Low temperature $^{125}Te\{^1H\}$ measurements yielded only a single resonance, consistent with the room temperature spectrum, and this further corroborates that the rotation is about the C3−C6 axis. If other rotational or conformational changes were responsible, the two Te atoms may find themselves in different chemical environments. The wide chemical shift range of ^{125}Te NMR makes it incredibly sensitive to small changes in the chemical environment. See the Supporting Information for low temperature ^{13}C and $^{125}Te\{^1H\}$.

Ultrafast Transient Absorption Spectroscopy. fsTA measurements were performed to interrogate the excited states of the dyes. Initial experiments were performed using either a 400 or 800 nm pump beam to irradiate aerated samples dissolved in acetonitrile, probing from 440 to 750 nm. Performing TA measurements with an 800 nm pump allowed for lower concentrations of the dyes and less excitation energy; permitting easier observation of any triplet transient absorption processes vide infra. No significant differences in the photophysics were observed between the 400 and 800 nm pump data (see the Supporting Information). It is important to note that no photodegradation was observed during these experiments as observed by monitoring the GSA of the samples before and after the TA measurements, and this is in contrast to other organic chromophores.

Generally, the dyes exhibited large, excited-state absorption (ESA) bands with maxima (λ_{ESA}) ranging from 469 to 608 nm, shifted to higher energy with respect to the GSA. The bands were relatively sharp with associated full-width-at-half-maxima ranging from 20 to 60 nm. Electronically, the excited-state and first reduced-state of the dyes are similar. This suggests that the transition of an electron to or from the singly occupied molecular orbital dominates this absorption.[38] Across the dye series, the wavelength maxima of the ESA bands were correlated with their respective GSA maxima. In general, the tellurium dyes have longer wavelength λ_{ESA} compared to their selenium analogues. The mixed chalcogen dyes, **T1.5-SeTePh** and **T5.5-SeTe^{t}Bu**, have λ_{ESA} approximately the average of their symmetric parent dyes. Additionally, trimethine dyes have shorter wavelength λ_{ESA} compared to their pentamethine analogues. These TA spectra returned to the baseline and were superimposable, indicative of population of a single excited state that cleanly returned to the ground state. The excited-state lifetimes were obtained by fitting λ_{ESA} decay traces to either mono- or bi-exponential decay kinetics with values ranging from roughly 80to 310 ps. The photophysical parameters of the dyes determined by TA experiments are summarized in Table 4. Due to insufficient GSA with 800 nm

Table 4. ESA and Lifetime Data from 800 nm Excitation fsTA in Acetonitrile

dye	λ_{ESA} (nm)	τ (ps)
T1-SePh	522	110
T1.5-SeTePh	539	108
T2-TePh	561	108
T3-Se3Th	517	104, 231
T4-Se2Th	538	62, 151
T5-Se^{t}Bu	469[a]	77[a]
T5.5-SeTe^{t}Bu	492	45, 123
T6-Te^{t}Bu	504	48, 140
P1-SePh	577	124
P2-TePh	608	89
P3-Se3Th	574	126
P4-Se2Th	601	94
P5-Se^{t}Bu	523	65, 269
P6-Te^{t}Bu	556	74, 245

[a]400 nm excitation data.

https://doi.org/10.1021/acs.organomet.2c00263
Organometallics 2022, 41, 2301−2316

excitation, data for **T5-Se^{t}Bu** are from 400 nm excitation. No tractable trends were found when examining structure−lifetime relationships. These short lifetimes, in conjunction with the small Stokes shifts observed in the emission spectra, suggest that the excited state is singlet in nature. This suggests that the excited states of all dyes behave similarly, and the chalcogen does not manifest in a significant heavy atom effect, where the Te-dyes access a triplet state to a greater extent than the Se-dyes.[39]

To provide further evidence for the singlet character of the excited states and suggest against a triplet transient absorption process, a comparison between aerated and freeze−pump−thaw degassed samples were performed along with NIR (840−1500 nm) TA measurements on an inclusive sample of the dyes. The spectral shape and lifetimes were identical, within experimental error, between aerated and freeze−pump−thaw degassed samples. This also held true for trimethine (Figure S135) and tellurium dyes (Figures S136 and S137). If a long-lived triplet transient process was operative, an ESA feature at lower energy from the GSA would be present. Thus, we posit that the rotation of the pyran ring relative to the methine backbone is the likely non-radiative path out of the excited state. This is consistent with our 77 K emission experiments previously discussed, where this non-radiative rotational pathway is attenuated, allowing more triplet state population.

We also carried out NIR TA measurements in an attempt to observe triplet-state absorption at longer wavelengths, but no peaks were found. Additionally, lifetimes did not change between the visible and NIR measurements. An example of NIR TA data is shown in Figure 15. NIR and visible TA lifetimes were within 15% error. The only feature present in the NIR TA measurements was the ground-state bleach (GSB) (see the Supporting Information).

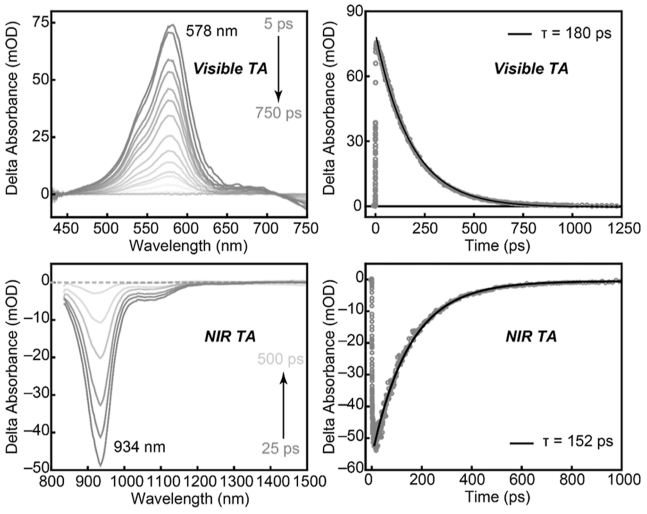

Figure 15. Comparison of visible and NIR fsTA spectra and decay traces of **P1-SePh**.

Singlet Oxygen Experiments. CPP dyes are reported to produce singlet oxygen through triplet state energy transfer with a quantum efficiency, ϕ_Δ, up to 0.12 in methanol.[2] These dyes have been extensively studied for their use as photosensitizers for photodynamic therapy.[2−6] Since we saw no evidence for significant population of triplet states at room temperature, we became curious about the relationship between these dyes and reactive oxygen species generated photochemically. To test whether the dyes of interest produced singlet oxygen, samples of **T6-Te^{t}Bu** in aerated 100% MeOH, aerated 50:50 MeOH/H_2O, and freeze−pump−thaw degassed 50:50 MeOH/H_2O were irradiated with a 450 nm CW laser (∼10−30 mW power). We then attempted to detect the direct phosphorescence of singlet oxygen at ∼1265 nm (Figure 16). In all samples, there was no detectable singlet oxygen emission.

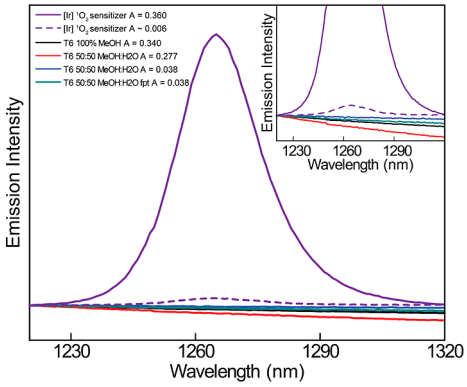

Figure 16. Singlet oxygen emission spectra of solutions of **T6-Te^{t}Bu** compared to a known singlet oxygen sensitizer [Ir(pbt)$_2$(acac)]. Absorbance recorded at 450 nm. The irradiation source was a 450 nm CW laser (∼10 mW power).

A new absorption band at ∼520 nm was observed in the aerated 50:50 MeOH/H_2O sample after irradiation with the high-powered CW laser (Figure 17). This data strongly suggest

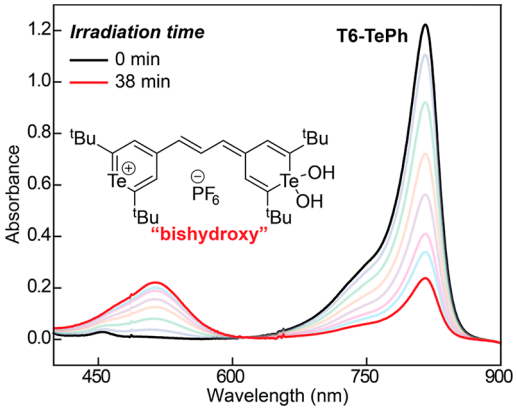

Figure 17. UV−vis spectra illustrating the consumption of CPP dye and formation of a bishydroxy species after 38 min of broadband irradiation of an aerated 50% MeOH aqueous sample of **T6-Te^{t}Bu**.

the formation of a Te(IV) bishydroxy species, which has been proposed in the literature.[7] The photolysis experiment in conjunction with the TA data suggests that these dyes do not access triplet-excited states in any appreciable amount and do not sensitize singlet oxygen with yields ∼12%, as was previously reported in this solvent mixture. These previous measurements were indirect with the evidence for singlet oxygen based on a reporter molecule, and the details of the experiment were not fully provided.[7] Aerated 100% MeOH samples of **T1-SePh** and **T2-TePh** were also tested and did not produce any singlet oxygen emission. Singlet oxygen quantum yields of related dyes and similar compounds have been determined through the reaction of $^1O_2$ with 1,3-

https://doi.org/10.1021/acs.organomet.2c00263
Organometallics 2022, 41, 2301−2316

diphenylbenzoisofuran (DPBF) along with other relative methods.[7,40,41] In addition to the spectral measurements previously discussed, a commonly used relative method for the determination of singlet oxygen quantum yields was performed on the dye. This method is selective and many ROS will contribute to an observed quantum yield.[42−45] When we compare the DPBF emission decrease in a known standard (methylene blue)/DPBF mixture to a CPP dye (**T6-Te^{t}Bu**)/DPBF mixture, we calculate a ϕ_Δ of 0.06 for **T6-Te^{t}Bu**. Because we do not observe singlet oxygen emission directly under the same conditions, we do not assign this as a singlet oxygen quantum yield, but rather some other pathway that generates ROS or even another interaction between the dye and DPBF.

Furthermore, samples of **T6-Te^{t}Bu** with and without water and oxygen were irradiated with a 14 W broadband LED lamp over 38 min and reactivity was monitored *via* UV−vis and NMR. The aerated 100% MeOH, freeze−pump−thaw degassed 100% MeOH, and freeze−pump−thaw-degassed 50:50 MeOH/H_2O samples all showed no spectral change after 38 min of irradiation. The aerated 50:50 MeOH/H_2O sample showed a decrease of the lambda max 813 nm with an increase of a new absorption band at 513 nm, as shown in Figure 17, the same behavior was observed with the high-powered CW laser irradiation. The new absorption band does not appear without the presence of both oxygen and water. This behavior agrees with the previously reported data,[7] where the new absorption band was attributed to the formation of a bishydroxy tellurium compound that was thought to be formed through the reaction with singlet oxygen produced by the dye. It is important to note that at STP, methanol has an order of magnitude more dissolved $^3O_2$ present compared to water.[46] If $^1O_2$ was generated and the cause of these spectral changes, one would expect to see this behavior most strongly in the 100% MeOH sample. In addition, an aerated 50:50 MeOH/H_2O sample of **T6-Te^{t}Bu** at NMR concentration was also irradiated with the 14 W broadband lamp. Dye resonances disappeared and new resonances appeared. The new species correspond to the previously reported resonances of the bishydroxy tellurium compound (Figure S18).[7] Therefore, the bishydroxy tellurium compound may form without singlet oxygen present and instead is formed by some other route, and we contend that a photoredox mechanism may better explain the observed phenomenon. This is a point of ongoing work in our laboratory.

Excited-State Dynamics. The excited state processes of these dyes are illustrated in Figure 18. The Franck−Condon transition at the lambda max corresponds to the HOMO−LUMO transition (*i.e.*, the dye S_0 to S_1 transition). At room temperature, these dyes relax from their S_1 state through either short-lived fluorescence or non-radiative decay. No measurable triplet state population due to intersystem crossing from the S_1 state to the T_1 state was observed. This results in the conspicuous lack of singlet oxygen sensitization and phosphorescence. Furthermore, the sub-300 ps lifetimes are too short to permit the diffusional bimolecular process.[47] We contend that the rotation observed by VT-NMR is a major contributor to the rapid non-radiative depopulation of the S_1 state. As such, intersystem crossing is unable to compete, consistent with the lack of observed triplet transient processes.

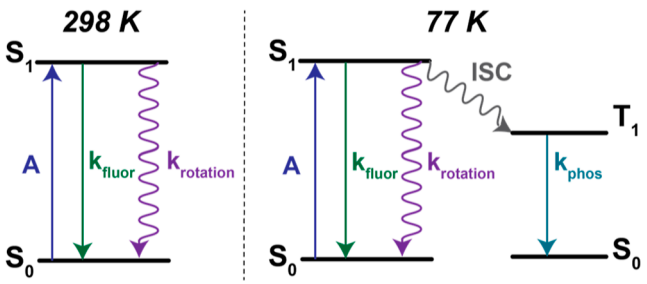

Figure 18. Jablonski diagram of the excited-state dynamics of CPP dyes at 298 and 77 K.

There is a notable change in excited-state dynamics at 77 K. The observation of phosphorescence at low temperatures supports that the rotational motion previously discussed (see Figure 12) has been shut down. As a result, intersystem crossing becomes competitive, thus populating the T_1 state (see Figure 18).

CONCLUSIONS

In concert, our results shed light upon the nuances of chalcogenopyrylium dyes. Through the use of electronic absorption and emission spectroscopies, electrochemical measurements, and DFT as well as TD-DFT calculations, we have established a complete discussion of the role of chalcogen identity, R-group, and methine backbone length on the electronic structure of chalcogenopyrylium dyes. We have established from VT-NMR experiments that rotation of the pyran ring relative to the methine backbone is facile at room temperature. This is the first systematic study of this rotation by NMR. Rotation about the methine backbone provides a rapid non-radiative pathway out of the excited state, consistent with the sub-300 ps lifetimes. This unexpected rotational phenomenon is a critical component to a complete discussion of the photophysical dynamics in CPP dyes. Our results bring into question the previously reported mechanism of formation of the bishydroxy complex, which was predicated upon the sensitization of singlet oxygen. This is an ongoing point of research in our laboratory and will be the focus of future articles.

EXPERIMENTAL SECTION

See the Supporting Information for complete experimental details.

Synthesis of T1-SePh.

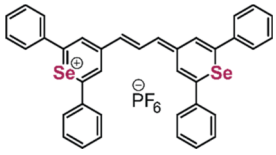

A mixture of 4-methyl-2,6-diphenylselenopyrylium hexafluorophosphate (100 mg, 0.22 mmol), 2-(2,6-diphenyl-4*H*-selenopyran-4-ylidene)acetaldehyde (81.5 mg, 0.24 mmol), and acetic anhydride (3.7 mL) was heated at 105 °C for 15 min, under nitrogen. After cooling to ambient temperature, the reaction mixture was diluted with CH_3CN (1.0 mL), followed by the addition of diethyl ether (10 mL) to precipitate the solid. The crude product was purified by a two-solvent recrystallization from 10% CH_3CN/diethyl ether to yield 158 mg (93%) of a green, crystalline solid. ^1H NMR (400 MHz, CD_2Cl_2): δ 8.60 (t, J = 13.3 Hz, 1H, methine), 7.90 (br s, 4H, pyran), 7.75−7.46 (m, 20H, phenyl), 6.84 (d, J = 13.3 Hz, 2H, methine); λ_{max} (CH_3CN) 793 nm (ε = 1.97(3) × 10^5 M^{-1}

https://doi.org/10.1021/acs.organomet.2c00263
Organometallics 2022, 41, 2301−2316

cm^{-1}); HRMS (ESI-FT-ICR MS) m/z: 631.0436 (calcd for $C_{37}H_{27}Se_2^+$ m/z: 631.0439).

Synthesis of T1.5-SeTePh.

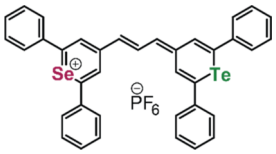

A mixture of 4-methyl-2,6-diphenyltelluropyrylium hexafluorophosphate (67.9 mg, 0.14 mmol), 2-(2,6-diphenyl-4*H*-selenopyran-4-ylidene)acetaldehyde (50.0 mg, 0.15 mmol), and acetic anhydride (2.8 mL) was heated at 105 °C for 100 s, under nitrogen. Chilling precipitated the crystalline product. The product was filtered and washed with diethyl ether to yield 99.8 mg (90%) of a dark maroon, crystalline solid. ^{1}H NMR (500 MHz, CD_2Cl_2): δ 8.68 (t, J = 13.3 Hz, 1H, methine), 7.91 (br s, 4H, pyran), 7.77−7.67 (m, 4H, phenyl), 7.67−7.50 (m, 16H, phenyl), 6.89 (dd, J = 29.5, 13.2 Hz, 2H, methine); λ_{max} (CH_3CN) 830 nm (ε = 1.78(3) × 10^5 M^{-1} cm^{-1}); HRMS (ESI-FT-ICR MS) m/z: 679.0316 (calcd for $C_{37}H_{27}SeTe^+$ m/z: 679.0332).

Synthesis of T2-TePh.

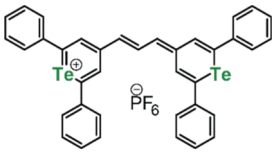

A mixture of 4-methyl-2,6-diphenyltelluropyrylium hexafluorophosphate (80.0 mg, 0.16 mmol), 2-(2,6-diphenyl-4*H*-telluropyran-4-ylidene)acetaldehyde (67.4 mg, 0.17 mmol), and acetic anhydride (2.7 mL) was heated at 105 °C for 13 min, under nitrogen. After cooling to ambient temperature, the reaction mixture was diluted with CH_3CN (1.0 mL), followed by the addition of diethyl ether (10 mL) to precipitate out solid. The crude product was purified by a two-solvent recrystallization from 10% CH_3CN/diethyl ether to yield 106 mg (77%) of a rust orange, crystalline solid. ^{1}H NMR (400 MHz, CD_2Cl_2): δ 8.77 (t, J = 13.1 Hz, 1H, methine), 7.94 (br s, 4H, pyran), 7.72−7.44 (m, 20H, phenyl), 6.92 (d, J = 13.1 Hz, 2H, methine); λ_{max} (CH_3CN) 868 nm (ε = 1.78(2) × 10^5 M^{-1} cm^{-1}); HRMS (ESI-FT-ICR MS) m/z: 727.01952 (calcd for $C_{37}H_{27}Te_2^+$ m/z: 727.0195).

Synthesis of T3-Se3Th.

A mixture of 4-methyl-2,6-di(thiophen-3-yl)selenopyrylium hexafluorophosphate (100 mg, 0.21 mmol), 2-(2,6-di-(thiophen-3-yl)-4*H*-selenopyran-4-ylidene)acetaldehyde (82.2 mg, 0.24 mmol), and acetic anhydride (4.0 mL) was heated at 105 °C for 15 min, under nitrogen. After cooling to ambient temperature, the reaction mixture was diluted with CH_3CN (1.0 mL), followed by the addition of diethyl ether (10 mL) to precipitate out solid. The crude product was purified by a two-solvent recrystallization from 10% CH_3CN/diethyl ether to yield 163 mg (95%) of a dark golden yellow, crystalline solid. ^{1}H NMR (500 MHz, CD_2Cl_2): δ 8.69 (t, J = 12.7 Hz, 1H, methine), 7.90 (br s, 4H, pyran), 7.67−7.34 (m, 12H, thiophene), 6.76 (d, J = 13.0 Hz, 2H, methine); λ_{max} (CH_3CN) 808 nm (ε = 2.03(7) × 10^5 M^{-1} cm^{-1}); ^{19}F{^{13}C} NMR (282 MHz, CD_2Cl_2): δ −71.53, −74.05, −150.73; HRMS (ESI-FT-ICR MS) m/z: 654.8687 (calcd for $C_{29}H_{19}S_4Se_2^+$ m/z: 654.8696).

Synthesis of T4-Se2Th.

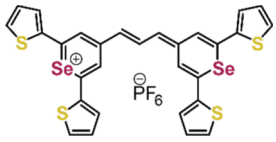

A mixture of 4-methyl-2,6-di(thiophen-2-yl)selenopyrylium hexafluorophosphate (100 mg, 0.21 mmol), 2-(2,6-di-(thiophen-2-yl)-4*H*-selenopyran-4-ylidene)acetaldehyde (82.2 mg, 0.24 mmol), and acetic anhydride (4.0 mL) was heated at 105 °C for 11 min, under nitrogen. After cooling to ambient temperature, the reaction mixture was diluted with CH_3CN (1.0 mL), followed by the addition of diethyl ether (10 mL) to precipitate out solid. The crude product was purified by a two-solvent recrystallization from 10% CH_3CN/diethyl ether to yield 149 mg (88%) of a dark turquoise, crystalline solid. ^{1}H NMR (500 MHz, CD_2Cl_2): δ 8.54 (t, J = 13.1 Hz, 1H, methine), 7.93−7.56 (m, 12H, thiophene), 7.26 (dd, J = 5.1, 3.7 Hz, 4H, pyran), 6.75 (d, J = 13.2 Hz, 2H, methine); λ_{max} (CH_3CN) 840 nm (ε = 1.56(5) × 10^5 M^{-1} cm^{-1}); HRMS (ESI-FT-ICR MS) m/z: 654.8691 (calcd for $C_{29}H_{19}S_4Se_2^+$ m/z: 654.8692).

Synthesis of T5-Se^{t}Bu.

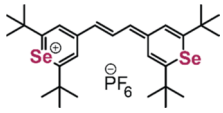

A mixture of 2,6-di-*tert*-butyl-4-methylselenopyrylium hexafluorophosphate (90.0 mg, 0.22 mmol), 2-(2,6-di-*tert*-butyl-4*H*-selenopyran-4-ylidene)acetaldehyde (69.0 mg, 0.24 mmol), and acetic anhydride (3.7 mL) were heated at 105 °C for 6 min, under nitrogen. After cooling to ambient temperature, the reaction mixture was diluted with CH_3CN (1.0 mL), followed by the addition of diethyl ether (10 mL) to precipitate out solid. The crude product was purified by a two-solvent recrystallization from 10% CH_3CN/diethyl ether to yield 96.5 mg (64%) of a metallic emerald, crystalline solid. ^{1}H NMR (400 MHz, CD_2Cl_2): δ 8.46 (t, J = 13.3 Hz, 1H, methine), 7.54 (br s, 4H, pyran), 6.56 (d, J = 13.3 Hz, 2H, methine), 1.47 (s, 36H, ^{t}Bu); λ_{max} (CH_3CN) 734 nm (ε = 2.074(9) × 10^5 M^{-1} cm^{-1}); HRMS (ESI-FT-ICR MS) m/z: 551.1691 (calcd for $C_{29}H_{43}Se_2^+$ m/z: 551.1691).

Synthesis of T5.5-SeTe^{t}Bu.

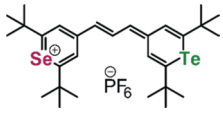

A mixture of 2,6-di-*tert*-butyl-4-methylselenopyrylium hexafluorophosphate (75.7 mg, 0.18 mmol), 2-(2,6-di-*tert*-butyl-4*H*-telluropyran-4-ylidene)acetaldehyde (69.4 mg, 0.20 mmol), and acetic anhydride (3.8 mL) was heated at 105 °C for 110 s. After cooling to ambient temperature, the crude reaction mixture was concentrated to dryness, diluted with CH_3CN (1.0 mL), and then, diethyl ether (10 mL) was added, and the mixture was placed in the freezer to precipitate out solid. The crystalline product was collected *via* filtration and

https://doi.org/10.1021/acs.organomet.2c00263
Organometallics 2022, 41, 2301−2316

washed with diethyl ether to yield 86.3 mg (64%) of a light golden green, crystalline solid. ^{1}H NMR (500 MHz, CD_2Cl_2): δ 8.58 (t, J = 13.3 Hz, 1H, methine), 7.58 (br s, 4H, pyran), 6.62 (dd, J = 30.8, 13.3 Hz, 2H, methine), 1.48 (s, 18H, ^{t}Bu) 1.46 (s, 18H, ^{t}Bu); λ_{max} (CH_3CN) 774 nm (ε = 2.12(2) × 10^5 M^{-1} cm^{-1}); HRMS (ESI-FT-ICR MS) m/z: 599.1559 (calcd for $C_{29}H_{43}SeTe^+$ m/z: 599.1582).

Synthesis of T6-Te^{t}Bu.

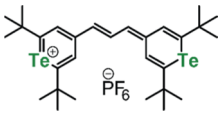

A mixture of 2,6-di-*tert*-butyl-4-methyltelluropyrylium hexafluorophosphate (157 mg, 0.34 mmol), 2-(2,6-di-*tert*-butyl-4*H*-telluropyran-4-ylidene)acetaldehyde (129 mg, 0.37 mmol), and acetic anhydride (5.7 mL) was heated at 105 °C for 15 min, under nitrogen. After cooling to ambient temperature, the reaction mixture was diluted with CH_3CN (1.0 mL), followed by the addition of diethyl ether (10 mL) to precipitate out solid. The crude product was purified by a two-solvent recrystallization from 10% CH_3CN/diethyl ether to yield 178 mg (67%) of a forest green, crystalline solid. ^{1}H NMR (400 MHz, CD_2Cl_2): δ 8.70 (t, J = 13.3 Hz, 1H, methine), 7.62 (br s, 4H, pyran), 6.68 (d, J = 13.3 Hz, 2H, methine), 1.46 (s, 36H, ^{t}Bu); ^{13}C NMR (126 MHz, CD_2Cl_2, −14 °C): δ 175.8, 174.5, 154.4, 140.9, 131.9, 131.6, 123.9, 43.02, 32.37; ^{13}C NMR (126 MHz, CD_2Cl_2, 25 °C): δ 175.5, 155.0, 141.4, 132.0, 128.5, 43.02, 32.37; ^{125}Te{^{1}H} (158 MHz, CD_2Cl_2): δ 734.92; λ_{max} (CH_3CN) 813 nm (ε = 2.08(2) × 10^5 M^{-1} cm^{-1}); HRMS (ESI-FT-ICR MS) m/z: 647.1446 (calcd for $C_{29}H_{43}Te_2^+$ m/z: 647.1457).

Synthesis of P1-SePh.

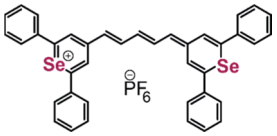

A mixture of 4-methyl-2,6-diphenylselenopyrylium hexafluorophosphate (150 mg, 0.33 mmol), *N*-((1*Z*,2*E*)-3-(phenylamino)allylidene)benzenaminium hexafluorophosphate (62.7 mg, 0.17 mmol), sodium acetate (27.0 mg, 0.33 mmol), acetic acid (1.03 mL), and acetic anhydride (1.03 mL) was heated at 90 °C for 25 min, under nitrogen. After cooling to ambient temperature, diethyl ether (10 mL) was added to precipitate out solid. The crude solid was collected by filtration and purified by a two-solvent recrystallization from 10% CH_3CN/diethyl ether to yield 80.8 mg (61%) of a dark mustard yellow, crystalline solid. ^{1}H NMR (500 MHz, CD_2Cl_2): δ 8.15 (t, J = 13.0 Hz, 2H, methine), ∼7.80 (br s, 4H, pyran), 7.76−7.61 (m, 8H, phenyl), 7.61−7.48 (m, 12H, phenyl), 6.84 (t, J = 12.5 Hz, 1H, methine), 6.71 (d, J = 13.6 Hz, 2H, methine); λ_{max} (CH_3CN) 911 nm (ε = 1.748(8) × 10^5 M^{-1} cm^{-1}); HRMS (ESI-FT-ICR MS) m/z: 657.0590 (calcd for $C_{39}H_{29}Se_2^+$ m/z: 657.0596).

Synthesis of P2-TePh.

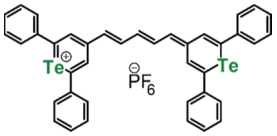

A mixture of 4-methyl-2,6-diphenyltelluropyrylium hexafluorophosphate (76.9 mg, 0.15 mmol), *N*-((1*Z*,2*E*)-3-(phenylamino)allylidene)benzenaminium hexafluorophosphate (28.1 mg, 0.08 mmol), sodium acetate (12.5 mg, 0.15 mmol), acetic acid (0.5 mL), and acetic anhydride (0.5 mL) was heated at 90 °C for 25−30 min. After cooling to ambient temperature, diethyl ether (10 mL) was added to precipitate out solid. The crude solid was collected *via* filtration and purified by a traditional recrystallization from CH_3CN heated to 75−80 °C to yield 26.5 mg (39%) of a gold, crystalline solid. ^{1}H NMR (500 MHz, CD_2Cl_2): δ 8.18 (t, J = 13.1 Hz, 2H, methine), 7.85 (br s, 4H, pyran), 7.69−7.45 (m, 20H, phenyl), 6.84 (dd, J = 31.1, 13.0 Hz, 3H, methine); λ_{max} (CH_3CN) 985 nm (ε = 9.33(4) × 10^4 M^{-1} cm^{-1}); HRMS (ESI-FT-ICR MS) m/z: 755.0309 (calcd for $C_{39}H_{29}Te_2^+$ m/z: 755.0376).

Synthesis of P3-Se3Th.

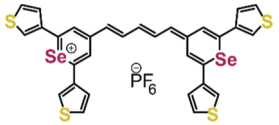

A mixture of 4-methyl-2,6-di(thiophen-3-yl)selenopyrylium hexafluorophosphate (150 mg, 0.32 mmol), *N*-((1*Z*,2*E*)-3-(phenylamino)allylidene)benzenaminium hexafluorophosphate (61.0 mg, 0.16 mmol), sodium acetate (26.3 mg, 0.32 mmol), acetic acid (1.0 mL), and acetic anhydride (1.0 mL) was heated to 90 °C for 35 min, under nitrogen. After cooling to ambient temperature, diethyl ether was added to precipitate out solid. The crude solid was collected *via* filtration and purified by a traditional recrystallization from CH_3CN heated to 75−80 °C to yield 104 mg (79%) of a brown solid. ^{1}H NMR (500 MHz, CD_2Cl_2): δ 8.11 (t, J = 13.0 Hz, 2H), 7.84 (m, 4H), 7.60 (br s, buried under baseline at 25 °C, 4H), 7.65−7.40 (m, 8H), 6.80 (t, J = 12.1 Hz, 1H), 6.67 (d, J = 13.4 Hz, 2H); λ_{max} (CH_3CN) 927 nm (ε = 1.16(1) × 10^5 M^{-1} cm^{-1}); HRMS (ESI-FT-ICR MS) m/z: 680.8840 (calcd for $C_{31}H_{21}S_4Se_2^+$ m/z: 680.8853).

Synthesis of P4-Se2Th.

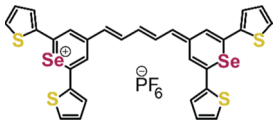

A mixture of 4-methyl-2,6-di(thiophen-2-yl)selenopyrylium hexafluorophosphate (100 mg, 0.21 mmol), *N*-((1*Z*,2*E*)-3-(phenylamino)allylidene)benzenaminium hexafluorophosphate (39.4 mg, 0.11 mmol), sodium acetate (17.5 mg, 0.21 mmol), acetic acid (0.67 mL), and acetic anhydride (0.67 mL) was heated at 90 °C for 25 min, under nitrogen. After cooling to ambient temperature, diethyl ether (10 mL) was added to precipitate out solid. The crude solid was purified by the slow evaporation of CH_3CN heated to 75−80 °C to yield 12 mg (14%) of a golden brown solid. ^{1}H NMR (500 MHz, CD_2Cl_2): δ 8.00 (t, J = 12.8 Hz, 2H, methine), ∼7.60 (br s, 4H, pyran), 7.62 (d, J = 5.0 Hz, 4H, thiophene), 7.55 (s, 4H, thiophene), 7.19 (dd, J = 5.0, 3.6 Hz, 4H, thiophene), 6.82 (t, 12.8 Hz, 1H, methine), 6.64 (d, J = 13.3 Hz, 2H, methine); λ_{max} (CH_3CN) 963 nm (ε = 1.17(2) × 10^5 M^{-1} cm^{-1}); HRMS (ESI-FT-ICR MS) m/z: 680.88355 (calcd for $C_{31}H_{21}S_4Se_2^+$ m/z: 680.88526).

https://doi.org/10.1021/acs.organomet.2c00263
Organometallics 2022, 41, 2301−2316

Synthesis of P5-Se^{t}Bu.

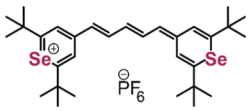

A mixture of 2,6-di-*tert*-butyl-4-methylselenopyrylium hexafluorophosphate (150 mg, 0.36 mmol), *N*-((1*Z*,2*E*)-3-(phenylamino)allylidene)benzenaminium hexafluorophosphate (68.7 mg, 0.18 mmol), sodium acetate (29.6 mg, 0.36 mmol), acetic acid (1.13 mL), and acetic anhydride (1.13 mL) was heated at 90 °C for 34 min, under nitrogen. After cooling to ambient temperature, diethyl ether (15 mL) was added to precipitate out solid. The crude solid was purified by a two-solvent recrystallization from 10% CH_3CN/diethyl ether to yield 73.4 mg (56%) of a gold, crystalline solid. ^{1}H NMR (400 MHz, CD_2Cl_2): δ 7.91 (t, J = 13.0 Hz, 2H, methine), 7.46 (br s, 4H, pyran), 6.67 (t, J = 12.5 Hz, 1H, methine), 6.50 (d, J = 13.6 Hz, 2H, methine), 1.45 (s, 36H, ^{t}Bu); λ_{max} (CH_3CN) 847 nm (ε = 1.451(8) × 10^5 M^{-1} cm^{-1}); HRMS (ESI-FT-ICR MS) m/z: 577.1846 (calcd for $C_{31}H_{45}Se_2^+$ m/z: 577.1848).

Synthesis of P6-Te^{t}Bu.

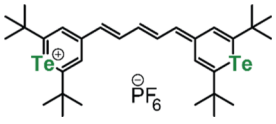

A mixture of 2,6-di-*tert*-butyl-4-methyltelluropyrylium hexafluorophosphate (150 mg, 0.32 mmol), *N*-((1*Z*,2*E*)-3-(phenylamino)allylidene)benzenaminium hexafluorophosphate (61.5 mg, 0.16 mmol), sodium acetate (26.5 mg, 0.32 mmol), acetic acid (1.0 mL), and acetic anhydride (1.0 mL) was heated at 90 °C for 32 min, under nitrogen. After cooling to ambient temperature, diethyl ether (15 mL) was added to precipitate out solid. The crude solid was purified by a two-solvent recrystallization from 10% CH_3CN/diethyl ether to yield 56.5 mg (43%) of a dark ruby red, crystalline solid. ^{1}H NMR (500 MHz, CD_2Cl_2): δ 8.02 (t, 2H, methine), 7.53 (br s, 4H, pyran), 6.88−6.42 (m, 3H, methine), 1.45 (s, 36H, ^{t}Bu); ^{125}Te{^{1}H} (158 MHz, CD_2Cl_2): δ 702.77; λ_{max} (CH_3CN) 926 nm (ε = 5.85(8) × 10^4 M^{-1} cm^{-1}); HRMS (ESI-FT-ICR MS) m/z: 673.1604 (calcd for $C_{31}H_{45}Te_2^+$ m/z: 673.1614).

■ ASSOCIATED CONTENT

Supporting Information

The Supporting Information is available free of charge at https://pubs.acs.org/doi/10.1021/acs.organomet.2c00263.

Synthetic procedure and spectroscopic characterization data (NMR, HR-MS, UV−Vis, Emission, and fsTA), electrochemical characterization, computational details, crystallographic data of T1-SePh, crystallographic data of T1.5-SeTePh, crystallographic data of T2-TePh, crystallographic data of T3-Se3Th, crystallographic data of T6-Te^{t}Bu, crystallographic data of P1-SePh, crystallographic data of P2-TePh, crystallographic data of P3−Se3Th, crystallographic data of P4−Se4Th, and crystallographic data of P5-Se^{t}Bu (PDF)

XYZ coordinates of optimized structures (XYZ)

Accession Codes

CCDC 2123679, 2123681−2123682, 2123685−2123686, 2123688−2123689, 2123691−2123692, and 2157317 contain the supplementary crystallographic data for this paper. These data can be obtained free of charge via www.ccdc.cam.ac.uk/data_request/cif, or by emailing data_request@ccdc.cam.ac.uk, or by contacting The Cambridge Crystallographic Data Centre, 12 Union Road, Cambridge CB2 1EZ, UK; fax: +44 1223 336033.

■ AUTHOR INFORMATION

Corresponding Author

Timothy R. Cook − *Department of Chemistry, University at Buffalo, The State University of New York, Buffalo, New York 14260, United States;* orcid.org/0000-0002-7668-8089; Email: trcook@buffalo.edu

Authors

Lauren E. Rosch − *Department of Chemistry, University at Buffalo, The State University of New York, Buffalo, New York 14260, United States;* orcid.org/0000-0002-6478-6415

Matthew R. Crawley − *Department of Chemistry, University at Buffalo, The State University of New York, Buffalo, New York 14260, United States;* orcid.org/0000-0002-2555-9543

Ryan M. O'Donnell − *DEVCOM Army Research Laboratory, Adelphi, Maryland 20783, United States;* orcid.org/0000-0002-3565-9783

Thomas N. Rohrabaugh, Jr. − *DEVCOM Army Research Laboratory, Adelphi, Maryland 20783, United States*

Trenton R. Ensley − *DEVCOM Army Research Laboratory, Adelphi, Maryland 20783, United States*

Thomas A. Sobiech − *Department of Chemistry, University at Buffalo, The State University of New York, Buffalo, New York 14260, United States;* orcid.org/0000-0002-8826-9375

Complete contact information is available at: https://pubs.acs.org/10.1021/acs.organomet.2c00263

Notes

The authors declare no competing financial interest.

■ ACKNOWLEDGMENTS

ESI-FT-ICR MS data were collected by Eric Jensen on a Bruker SolariXR FT-ICRMS purchased with NIH S10 RR029517, a part of the UB CIC. Bruker AVANCE NEO 500 MHz NMR purchased with NSF CHE-2018160, a part of the UB NMR center. The authors thank SUNY Fredonia for the use of their X-ray diffractometer, Dr. Samantha N. MacMillan for collecting some crystallographic data sets reported in this paper, and Heshali Welgama for electrochemistry discussions. Computational work was performed in part at the University at Buffalo's Center for Computational Research. This work was supported by NSF Award #1800288 and the Army Research Laboratory through cooperative agreement W911NF1920196.

■ REFERENCES

(1) Detty, M. R.; McKelvey, J. M.; Luss, H. R. Tellurapyrylium dyes. 2. The electron-donating properties of the chalcogen atoms to the chalcogenapyrylium nuclei and their radical dications, neutral radicals, and anions. *Organometallics* **1988**, *7*, 1131−1147.

(2) Detty, M. R.; Merkel, P. B. Chalcogenapyrylium dyes as potential photochemotherapeutic agents. Solution studies of heavy atom effects on triplet yields, quantum efficiencies of singlet oxygen generation, rates of reaction with singlet oxygen, and emission quantum yields. *J. Am. Chem. Soc.* **1990**, *112*, 3845−3855.

(3) Detty, M. R.; Merkel, P. B.; Hilf, R.; Gibson, S. L.; Powers, S. K. Chalcogenapyrylium dyes as photochemotherapeutic agents. 2. Tumor uptake, mitochondrial targeting, and singlet-oxygen-induced inhibition of cytochrome c oxidase. *J. Med. Chem.* **1990**, *33*, 1108−1116.
(4) Leonard, K. A.; Nelen, M. I.; Anderson, L. T.; Gibson, S. L.; Hilf, R.; Detty, M. R. 2,4,6-Triarylchalcogenopyrylium Dyes Related in Structure to the Antitumor Agent AA1 as in Vitro Sensitizers for the Photodynamic Therapy of Cancer. *J. Med. Chem.* **1999**, *42*, 3942−3952.
(5) Leonard, K. A.; Hall, J. P.; Nelen, M. I.; Davies, S. R.; Gollnick, S. O.; Camacho, S.; Oseroff, A. R.; Gibson, S. L.; Hilf, R.; Detty, M. R. A Selenopyrylium Photosensitizer for Photodynamic Therapy Related in Structure to the Antitumor Agent AA1 with Potent in Vivo Activity and No Long-Term Skin Photosensitization. *J. Med. Chem.* **2000**, *43*, 4488−4498.
(6) Bellnier, D. A.; Young, D. N.; Detty, M. R.; Camacho, S. H.; Oseroff, A. R. pH-Dependent Chalcogenopyrylium Dyes as Potential Sensitizers for Photodynamic Therapy: Selective Retention in Tumors by Exploiting pH Differences between Tumor and Normal Tissue. *Photochem. Photobiol.* **1999**, *70*, 630−636.
(7) Detty, M. R.; Merkel, P. B.; Powers, S. K. Tellurapyrylium dyes as photochemotherapeutic agents. Surprising tellurium atom effects for the generation of rates of reaction with singlet oxygen. *J. Am. Chem. Soc.* **1988**, *110*, 5920−5922.
(8) Walstad, D. L.; Brown, J. T.; Powers, S. K. The effect of a chalcogenapyrylium dye with and without photolysis on mitochondrial function in normal and tumor cells. *Photochem. Photobiol.* **1989**, *49*, 285−291.
(9) Bedics, M. A.; Mulhern, K. R.; Watson, D. F.; Detty, M. R. Synthesis and Photoelectrochemical Performance of Chalcogenopyrylium Monomethine Dyes Bearing Phosphonate/Phosphonic Acid Substituents. *J. Org. Chem.* **2013**, *78*, 8885−8891.
(10) Bedics, M. A.; Kearns, H.; Cox, J. M.; Mabbott, S.; Ali, F.; Shand, N. C.; Faulds, K.; Benedict, J. B.; Graham, D.; Detty, M. R. Extreme red shifted SERS nanotags. *Chem. Sci.* **2015**, *6*, 2302−2306.
(11) Harmsen, S.; Bedics, M. A.; Wall, M. A.; Huang, R.; Detty, M. R.; Kircher, M. F. Rational design of a chalcogenopyrylium-based surface-enhanced resonance Raman scattering nanoprobe with attomolar sensitivity. *Nat. Commun.* **2015**, *6*, 6570.
(12) Kearns, H.; Bedics, M. A.; Shand, N. C.; Faulds, K.; Detty, M. R.; Graham, D. Sensitive SERS nanotags for use with 1550 nm (retina-safe) laser excitation. *Analyst* **2016**, *141*, 5062−5065.
(13) Kearns, H.; Sengupta, S.; Sasselli, I. R.; Bromley, L., III; Faulds, K.; Tuttle, T.; Bedics, M. A.; Detty, M. R.; Velarde, L.; Graham, D.; Smith, W. E. Elucidation of the bonding of a near infrared dye to hollow gold nanospheres—a chalcogen tripod. *Chem. Sci.* **2016**, *7*, 5160−5170.
(14) Nicolson, F.; Jamieson, L. E.; Mabbott, S.; Plakas, K. V.; Shand, N. C.; Detty, M. R.; Graham, D.; Faulds, K. Towards establishing a minimal nanoparticle concentration for applications involving surface enhanced spatially offset resonance Raman spectroscopy (SESORRS) in vivo. *Analyst* **2018**, *143*, 5358−5363.
(15) Pala, L.; Mabbott, S.; Faulds, K.; Bedics, M. A.; Detty, M. R.; Graham, D. Introducing 12 new dyes for use with oligonucleotide functionalised silver nanoparticles for DNA detection with SERS. *RSC Adv* **2018**, *8*, 17685−17693.
(16) Plakas, K.; Rosch, L. E.; Clark, M. D.; Adbul-Rashed, S.; Shaffer, T. M.; Harmsen, S.; Gambhir, S. S.; Detty, M. R. Design and evaluation of Raman reporters for the Raman-silent region. *Nanotheranostics* **2022**, *6*, 1−9.
(17) Detty, M. R.; Murray, B. J. Telluropyrylium dyes. 1. 2,6-Diphenyltelluropyrylium dyes. *J. Org. Chem.* **1982**, *47*, 5235−5239.
(18) Schreiber, M.; Buß, V.; Fülscher, M. P. The electronic spectra of symmetric cyanine dyes: A CASPT2 study. *Phys. Chem. Chem. Phys.* **2001**, *3*, 3906−3912.
(19) Ohulchanskyy, T. Y.; Gannon, M. K.; Ye, M.; Skripchenko, A.; Wagner, S. J.; Prasad, P. N.; Detty, M. R. ″Switched-On″ Flexible Chalcogenopyrylium Photosensitizers. Changes in Photophysical Properties upon Binding to DNA. *J. Phys. Chem. B* **2007**, *111*, 9686−9692.
(20) Hofer, L. J. E.; Grabenstetter, R. J.; Wiig, E. O. The Fluorescence of Cyanine and Related Dyes in the Monomeric State1. *J. Am. Chem. Soc.* **1950**, *72*, 203−209.
(21) Piontkowski, Z.; Mark, D. J.; Bedics, M. A.; Sabatini, R. P.; Mark, M. F.; Detty, M. R.; McCamant, D. W. Excited state torsional processes in chalcogenopyrylium monomethine dyes. *J. Phys. Chem. A* **2019**, *123*, 8807−8822.
(22) Detty, M. R. Evidence in support of the Corey-Kahn mechanism of quenching of singlet oxygen with organometallic compounds. Oxophilicity and rates of intersystem crossing in organochalcogen compounds. *Organometallics* **1992**, *11*, 2310−2312.
(23) Detty, M. R.; Gibson, S. L. Tellurapyrylium dyes as catalysts for oxidations with hydrogen peroxide and as scavengers of singlet oxygen. Dihydroxytelluranes as mild oxidizing agents. *Organometallics* **1992**, *11*, 2147−2156.
(24) Detty, M. R.; Young, D. N.; Williams, A. J. A Mechanism for Heteroatom Scrambling in the Synthesis of Unsymmetrical Chalcogenopyrylium Trimethine Dyes. *J. Org. Chem.* **1995**, *60*, 6631−6634.
(25) Panda, J.; Virkler, P. R.; Detty, M. R. A Comparison of Linear Optical Properties and Redox Properties in Chalcogenopyrylium Dyes Bearing Ortho-Substituted Aryl Substituents and tert-Butyl Substituents. *J. Org. Chem.* **2003**, *68*, 1804−1809.
(26) Matichak, J. D.; Hales, J. M.; Ohira, S.; Barlow, S.; Jang, S.-H.; Jen, A. K.-Y.; Brédas, J.-L.; Perry, J. W.; Marder, S. R. Using End Groups to Tune the Linear and Nonlinear Optical Properties of Bis(dioxaborine)-Terminated Polymethine Dyes. *ChemPhysChem* **2010**, *11*, 130−138.
(27) Bedics, M. A. Chalcogenopyrylium Dyes with Anchors to Nanoparticle and Semiconductor Surfaces. Ph.D. Thesis, University at Buffalo, State University of New York, 2015.
(28) Plakas, K. H. On the Synthesis of Novel Dyes for Biomedical Imaging using Surface-Enhanced Raman Spectroscopy. Ph.D. Thesis, University at Buffalo, The State University of New York, 2019.
(29) Getmanenko, Y. A.; Allen, T. G.; Kim, H.; Hales, J. M.; Sandhu, B.; Fonari, M. S.; Suponitsky, K. Y.; Zhang, Y.; Khrustalev, V. N.; Matichak, J. D.; Timofeeva, T. V.; Barlow, S.; Chi, S.-H.; Perry, J. W.; Marder, S. R. Linear and Third-Order Nonlinear Optical Properties of Chalcogenopyrylium-Terminated Heptamethine Dyes with Rigid, Bulky Substituents. *Adv. Funct. Mater.* **2018**, *28*, 1804073.
(30) Müller, P. *Crystal Structure Refinement: A Crystallographer's Guide to SHELXL*; Oxford University Press, 2008.
(31) Chibani, S.; Le Guennic, B.; Charaf-Eddin, A.; Laurent, A. D.; Jacquemin, D. Revisiting the optical signatures of BODIPY with ab initio tools. *Chem. Sci.* **2013**, *4*, 1950−1963.
(32) Sawada, G. A.; Raub, T. J.; William Higgins, J.; Brennan, N. K.; Moore, T. M.; Tombline, G.; Detty, M. R. Chalcogenopyrylium dyes as inhibitors/modulators of P-glycoprotein in multidrug-resistant cells. *Bioorg. Med. Chem.* **2008**, *16*, 9745−9756.
(33) Grimme, S.; Neese, F. Double-hybrid density functional theory for excited electronic states of molecules. *J. Chem. Phys.* **2007**, *127*, 154116.
(34) Drago, R. S.; Corden, B. B. Spin-pairing model of dioxygen binding and its application to various transition-metal systems as well as hemoglobin cooperativity. *Acc. Chem. Res.* **1980**, *13*, 353−360.
(35) Reich, H. J. WINDNMR. *J. Chem. Educ., Software* **1996**, *3D*, 2.
(36) Neese, F.; Wennmohs, F.; Becker, U.; Riplinger, C. The ORCA quantum chemistry program package. *J. Chem. Phys.* **2020**, *152*, 224108.
(37) Detty, M. R.; Luss, H. R. Tellurapyrylium dyes. 3. Oxidative halogen addition and tellurium-halogen exchange. *Organometallics* **1986**, *5*, 2250−2256.
(38) Brown, A. M.; McCusker, C. E.; McCusker, J. K. Spectroelectrochemical identification of charge-transfer excited states in transition metal-based polypyridyl complexes. *Dalton Trans* **2014**, *43*, 17635−17646.

https://doi.org/10.1021/acs.organomet.2c00263
Organometallics 2022, 41, 2301−2316

(39) Detty, M. R. Heavy Atom Effects in Tellurapyrylium Dyes Useful in Photodynamic Therapy and Catalytic Generation of H2O2. *Phosphorus, Sulfur Silicon Relat. Elem.* **1992**, *67*, 383−404.
(40) Lutkus, L. V.; Rickenbach, S. S.; McCormick, T. M. Singlet oxygen quantum yields determined by oxygen consumption. *J. Photochem. Photobiol., A* **2019**, *378*, 131−135.
(41) Latch, D. E. The Role of Singlet Oxygen in Surface Water Photochemistry. In *Surface Water Photochemistry*; Calza, C., Vione, D., Ed.; Royal Society of Chemistry, 2016.
(42) Young, R. H.; Martin, R. L.; Chinh, N.; Mallon, C.; Kayser, R. H. Substituent Effects in Dye-sensitized Photooxidation Reactions of Furans. *Can. J. Chem.* **1972**, *50*, 932−938.
(43) Bhattacharyya, K.; Das, P. K. Quantitative aspects of all-trans-retinol singlet and triplet quenching by oxygen. *Chem. Phys. Lett.* **1985**, *116*, 326−332.
(44) Ding, H.-Y.; Wang, X.-S.; Song, L.-Q.; Chen, J.-R.; Yu, J.-H.; Chao-Li, L.; Zhang, B.-W. Aryl-modified ruthenium bis(terpyridine) complexes: Quantum yield of 1O2 generation and photocleavage on DNA. *J. Photochem. Photobiol., A* **2006**, *177*, 286−294.
(45) Albani, B. A.; Peña, B.; Leed, N. A.; de Paula, N. A. B. G.; Pavani, C.; Baptista, M. S.; Dunbar, K. R.; Turro, C. Marked Improvement in Photoinduced Cell Death by a New Tris-heteroleptic Complex with Dual Action: Singlet Oxygen Sensitization and Ligand Dissociation. *J. Am. Chem. Soc.* **2014**, *136*, 17095−17101.
(46) Pegis, M. L.; Wise, C. F.; Martin, D. J.; Mayer, J. M. Oxygen Reduction by Homogeneous Molecular Catalysts and Electrocatalysts. *Chem. Rev.* **2018**, *118*, 2340−2391.
(47) Gauglitz, G. Chapter 2—Photophysical, Photochemical and Photokinetic Properties of Photochromic Systems. *Photochromism*; Dürr, H., Bouas-Laurent, H., Eds.; Elsevier Science: Amsterdam, 2003; pp 15−63.

https://doi.org/10.1021/acs.organomet.2c00263
Organometallics 2022, 41, 2301−2316